Materials Science & Engineering C 118 (2021) 111436

Contents lists available at ScienceDirect

Materials Science & Engineering C

journal homepage: www.elsevier.com/locate/msec

Evaluation of in vitro corrosion resistance and in vivo osseointegration properties of a FeMnSiCa alloy as potential degradable implant biomaterial

Lucia Carmen Trincă[a], Liviu Burtan[b,*], Daniel Mareci[c,1], Bibiana M. Fernández-Pérez[d,2], Iulian Stoleriu[e], Teodor Stanciu[f], Sergiu Stanciu[f], Carmen Solcan[g], Javier Izquierdo[d,h], Ricardo M. Souto[d,h,**]

[a] Exact Sciences Department, "Ion Ionescu de la Brad" University of Agricultural Sciences and Veterinary Medicine, Faculty of Horticulture, Str. Aleea M. Sadoveanu, no. 3, 700490, Iasi, Romania
[b] Clinics Department, "Ion Ionescu de la Brad" University of Agricultural Sciences and Veterinary Medicine, Faculty of Veterinary Medicine, Str. Aleea M. Sadoveanu, no. 8, 700489, Iasi, Romania
[c] Department of Chemical Engineering, Technical University "Gheorghe Asachi" of Iasi, Faculty of Chemical Engineering and Environmental Protection, D. Mangeron, Iasi, 700050, Romania
[d] Department of Chemistry, Universidad de La Laguna, Avda. Astrofísico Francisco Sánchez s/n, E-38200 La Laguna, Tenerife, Canary Islands, Spain
[e] Faculty of Mathematics, "Alexandru Ioan Cuza" University of Iasi, Bd. Carol I, No. 11, 700506, Iasi, Romania
[f] Faculty of Materials Science and Engineering, "Gheorghe Asachi" Technical University of Iasi, Str. Prof. dr. doc. Dimitrie Mangeron, 67, 70005, Iasi, Romania
[g] Preclinics Department, "Ion Ionescu de la Brad" University of Agricultural Sciences and Veterinary Medicine, Faculty of Veterinary Medicine, Str. Aleea M. Sadoveanu, no. 8, 700489, Iasi, Romania
[h] Institute of Material Science and Nanotechnology, Universidad de La Laguna, P.O. Box 456, E-38200 La Laguna, Tenerife, Canary Islands, Spain

ARTICLE INFO

Keywords:
Biodegradable implant materials
Surface characterization
Corrosion resistance
FeMnSiCa alloy
FeMnSi alloy
Osseointegration

ABSTRACT

In vitro electrochemical characterization and in vivo implantation in an animal model were employed to evaluate the degradation behaviour and the biological activity of FeMnSi and FeMnSiCa alloys obtained using UltraCast (Ar atmosphere) melting. Electrochemical characterization was based on open circuit potential measurement, electrochemical impedance spectroscopy and potentiodynamic polarization techniques while the alloys were immersed in Ringer's solution at 37 °C for 7 days. Higher corrosion rates were measured for the Ca-containing material, resulting from inefficient passivation of the metal surface by oxy-hydroxide products. In vivo osseointegration was investigated on a tibia implant model in rabbits by referring to a standard control (*AISI 316 L*) stainless steel using standard biochemical, histological and radiological methods of investigation. Changes in the biochemical parameters were related to the main stages of the bone defect repair, whereas implantation of the alloys in rabbit's tibia provided the necessary mechanical support to the injured bone area and facilitated the growth of the newly connective tissue, as well as osteoid formation and mineralization, as revealed by either histological sections or computed tomography reconstructed images and validated by the bone morphometric indices. The present study highlighted that the FeMnSiCa alloy promotes better osteoinduction and osseconduction processes when compared to the base FeMnSi alloy or with *AISI 316 L*, and in vivo degradation rates correlate well with corrosion resistance measurements in Ringer's solution.

* Corresponding author.
** Correspondence to: Ricardo M. Souto, Department of Chemistry, Universidad de La Laguna, Avda. Astrofísico Francisco Sánchez s/n, E-38200 La Laguna, Tenerife, Canary Islands, Spain.
E-mail addresses: lctrinca@uaiasi.ro (L.C. Trincă), blmv2018@yahoo.com (L. Burtan), danmareci@yahoo.com (D. Mareci), bibiana@kth.se (B.M. Fernández-Pérez), stoleriu@yahoo.com (I. Stoleriu), teddy.stanciu16@gmail.com (T. Stanciu), sergiustanciu@yahoo.com (S. Stanciu), carmensolcan@yahoo.com (C. Solcan), jizquier@ull.edu.es (J. Izquierdo), rsouto@ull.edu.es (R.M. Souto).
[1] Deceased on January 8, 2017.
[2] Current address: School of Engineering Science in Chemistry, Biotechnology and Health, Royal Institute of Technology, Teknikringen 30, 10044 Stockholm, Sweden.

https://doi.org/10.1016/j.msec.2020.111436
Received 27 March 2020; Received in revised form 1 August 2020; Accepted 23 August 2020
Available online 25 August 2020

1. Introduction

An ideal biodegradable material should be biocompatible with bone tissue, sufficiently porous to stimulate bone induction, with a stable structure during the healing period to ensure osseointegration, but easily resorbable thereafter to leave no harmful traces in the body [1,2]. Iron-based biodegradable materials are attracting interest because in vivo tests have shown that pure iron implants do not show toxicity effects, neither inflammation processes [3]. In addition, iron-based alloys have an excellent mechanical behaviour, in addition to being inexpensive likewise stainless steel [4–8]. The strength and rate of degradation rate of pure Fe increases in alloys that combine Mn with Fe [9–12]. On the other hand, Si is an essential trace element for bone development that is involved in osteogenesis and collagen synthesis [13–17]. The addition of Ca can increase the bioactivity of the basic alloy, both by enhancing interactions at the implant-bone interface and by promoting the activation of osteoblasts [18–24].

The main hindrance for iron-based alloys to be employed for the manufacturing of biodegradable implants is the slow degradation rate of these materials [4]. Thus, Fe-Mn alloys, exhibit degradation rates at least one order of magnitude smaller than magnesium-based alloys [15,19,25]. Work in progress focuses on developing new iron-manganese based materials with lower corrosion resistance and higher degradation rates, by testing new alloy characteristics when other elements are added (i.e., Ca, Co, Mg, Si, V), and subsequently determine their optimal practical utility [1–4,6,8–12]. Recently, a FeMnSi (master) alloy was proposed by our group as alloplastic graft material for bone implants that evidenced a higher bone restoration process when compared to a standard/control implant after evaluation of its mechanical and physicochemical properties from in vitro corrosion assays and in vivo biodegradation tests in a rat tibia bone model [15]. These findings led us to consider the FeMnSi master alloy as an efficient and inexpensive biomaterial candidate for manufacturing implants for individuals that require a long recovery period. A small addition of Ca (1 wt.%) to FeMnSi should improve the functional properties of the master alloy, by upgrading the shape memory control of the master FeMnSi alloy through MnSi shape control [20,22], and by improving the corrosion characteristics of the alloy, through the promotion of a generalized corrosion process (i.e., a more homogeneous degradation rate) on the surface of the alloy [16,23], whereas facilitating the formation of hydroxyapatite [24].

In this work, the microalloying of an Fe10Mn6Si alloy by adding 1 wt.% Ca was investigated as a candidate material for bone implants by performing in vitro corrosion resistance tests as well as in vivo tests, and characterizing the surface of the samples after implantation. The main objective of this work was to evaluate and compare the degradation rates, corrosion mechanisms and osseointegration processes of the Fe10Mn6Si alloy with 1 wt.% added Ca (which will be named hereafter FeMnSiCa), with those of the unmodified Fe10Mn6Si (which will be named hereafter FeMnSi). Electrochemical characterization was performed in a simulated body fluid as corrosive environment, whereas in vivo tests were conducted in rabbit tibiae through cross-examined biochemical, histological and computed tomography (CT) investigations. The surface morphology and composition of the FeMnSiCa and FeMnSi specimens were investigated by scanning electron microscopy (SEM) and energy dispersive X-ray spectroscopy (EDS). In addition, the relationship between in vitro corrosion resistance characterization and in vivo performance was also discussed in order to evaluate the potential of FeMnSiCa alloys for biomedical application.

2. Materials and methods

2.1. Materials

The master Fe10Mn6Si alloy was produced by melting the high-purity metallic elements (i.e., Fe 99.99%, Mn 99.98% and Si 99.9%) in an electric arc furnace (RAV MRF ABJ_900, Allenstown, NY, USA). Details on the fabrication, as well as the structural and surface characterization of the as cast alloy, have been reported elsewhere [16,26]. Ca was added within 1 wt.% by the use of a vacuum induction furnace (UltraCast, Ronkonkoma, NY, USA) in a ceramic crucible [23]. The casted material was melted and annealed in a fluid bed of sand at 1050 °C for 300 min, then cooled along with the sand in which it was heated to obtain a homogenous solid solution and thus reducing the heating fragility induced by the hot deformation process.

2.2. Surface characterization

The morphological characterization of the implanted surfaces was carried out by scanning electron microscopy (SEM, model Vega II LMH, provided with a SE detector, Tescan, Brno, Czech Republic), while the chemical analysis of the surface of the material was performed by EDS (model XFlash with PB-ZAF Esprit software, Bruker, Billerica, MA, USA). MATLAB software [27] was employed for 2D- and 3D-reconstruction of the images of the plot surface profiles.

2.3. In vitro electrochemical characterization

FeMnSi and FeMnSiCa ingots were cut into small strips and mounted into a resin sleeve (Epofix kit, Struers, Ballerup, Denmark) to offer a flat surface for electrochemical tests, while the metal was allowed to protrude at the rear of the sleeve for electrical connection. The exposed areas were determined under microscope, namely 0.23 cm^2 for FeMnSi, and 0.35 cm^2 for the FeMnSiCa samples, respectively. The samples were abraded with silicon carbide paper down to 4000 grit, thoroughly rinsed with Millipore deionized water (resistivity, 18 MΩ·cm), and sonicated in ethanol for 15 min. Electrochemical tests were performed in Ringer's solution in order to simulate the corrosive aggressiveness of the physiological media. Ringer's solution was prepared from analytical grade reagents and Millipore deionized water. The composition of the Ringer's solution was 8.5 g/L NaCl, 0.40 g/L KCl and 0.34 g/L $CaCl_2{\cdot}2H_2O$. The temperature of the electrochemical cell was maintained at 37 ± 1 °C.

The alloy sample surrounded by the resin sleeve was placed upwards in the electrochemical cell, with a platinum grid and a saturated calomel electrode (SCE) serving as auxiliary and reference electrode, respectively. The electrochemical cell was placed inside a Faraday cage. Measurements were conducted using an EG&G Princeton Applied Research model 2263 potentiostat/galvanostat (AMETEK, Berwyn, PA, USA). Samples were initially left at their open circuit potential (OCP) for 1 h in order to develop a quasi-stable potential value. Electrochemical impedance spectroscopy (EIS) measurements were performed with the samples still unbiased at their open circuit potential in the test electrolyte, after 1 h, 1 day, and 1 week of immersion in Ringer's solution at 37 °C. EIS data were conducted by applying a sine wave perturbation at frequencies between 20 kHz and 1 mHz, with amplitude of ± 10 mV. The data quality acquisition was established in 15 cycles at each frequency, thus providing good signal-to-noise ratios at all frequencies. The impedance spectra were modelled in terms of an equivalent circuit by using Yeum's *ZSimpWin 2.00* software [28]. Finally, linear polarization tests were performed after 1 week of immersion, namely Tafel analysis, within the potential range between −200 and +200 mV vs. OCP, at scan rate 1 mV/s.

2.4. Evaluation of in vivo osseointegration

Three groups of rabbits (3 months of age, approximately 1.3 kg), received by surgery on the tibial crest (Fig. 1) an implanted specimen of parallelepiped shape (25 mm × 2.5 mm × 0.5 mm), either of the new alloys under investigation (i.e., FeMnSiCa and FeMnSi) or a control (AISI 316 L stainless steel). During the experiment, the animals were housed with free access to food and water in accordance with the

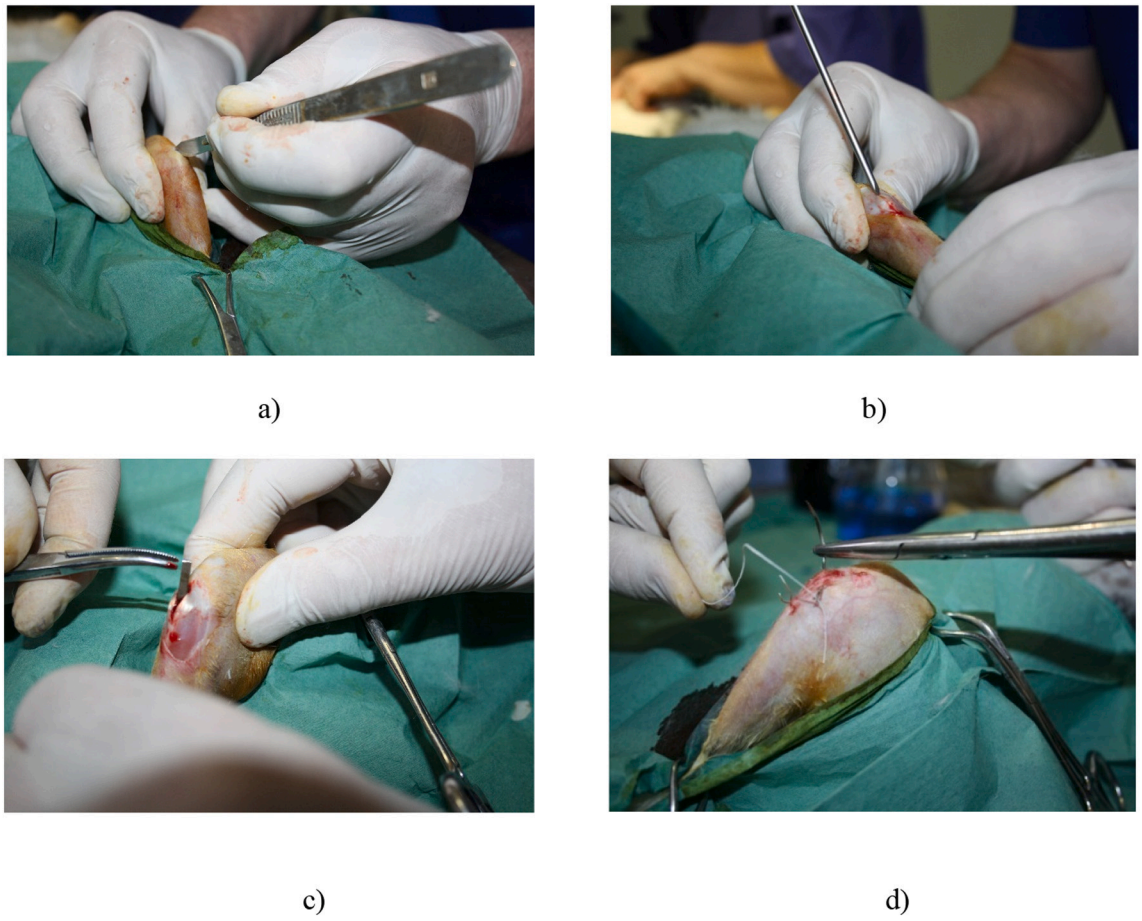

Fig. 1. Main stages of the tibia implant surgery in a rabbit.

ISO10993-2:2006 standard on animal welfare [29]. The experimental model was carried out for four weeks (28 days).

The evaluation of the implant osseointegration process, during the four weeks, involved a general evaluation of the health status of the rabbits from the experimental groups by permanent clinical control and weekly blood sample collection/analysis. The bone restoration process was monitored by the team of specialists (surgeons and clinicians) at the Faculty of Veterinary Medicine (FMV) Iasi after 2 and 4 weeks by X-rays that evidenced a normal evolution of bone recovery (see Supporting Information). Histological evaluation involved an intermediate test analysis at 2 weeks post-implantation, while at 4 weeks (at the end of the experiment), the major evaluation involved both CT and histomorphology investigations.

The implantation procedure was performed by the FMV Iasi surgical team under standard sterile conditions. Before surgery, all the rabbits were subjected to clinical checks. The anesthetic protocol used a mixture of ketamine hydrochloride-xylazine mixture and consisted in intramuscular administration of xylazine bio 2%, inj. ad us vet (0.4 mL/kg body weight), as the main analgesic, sedative, and 10 min later a muscle relaxant compound, a 10% ketamine solution (0.7 mL/kg body weight) as the main general anesthetic compound.

The intervention surface was prepared by shaving with an electric razor an area for twice the size of the planned surgical field. Skin disinfection was done with Betadine 1%. The animal was draped with a sterile, impermeable covering surgical field, that was fixed with clamps, to properly isolate the disinfected area. A 4 cm in length, straight incision was performed on the skin area above the palpated tibial crest (see Fig. 1a). After incision of the skin, the tibial crest was carefully exposed.

A cylindrical shape perforation (30 mm length, 3 mm diameter) was performed starting 0.5 cm below the proximal extremity of the tibial crest, with an electric surgical drill which was oriented to ensure access to the medullary channel (cf. Fig. 1b). Before insertion of the implants, the surgical perforation was washed with saline solution to remove any bone shards. The implant was inserted with the aid of the hemostatic pencil (see Fig. 1c) in the surgical cavity created in the tibia crest and pressed into the medullary canal to achieve primary stability until it was fixed by ensuring an oblique disposition.

The surgical wound of the different layers of soft tissues was closed with suture in separate threads (as it is shown in Fig. 1d), using resorbable threads No. 4/0 for the suture of the periosteum (to better assure stabilization of the implant) and non-absorbable threads No. 2/0, which were removed after 10 days, for suturing the skin and underlying tissues. The surgical procedure was performed in 30 min. To prevent wound infection, Enroxil 5% (0.1 mL/kg body weight) was administered intramuscularly for 3 days.

At the end of the experimental period, to provide euthanasia, the animals were previously anesthetized according to the same protocol presented above. The procedure of euthanasia involved an intrapulmonary injection of T-61 solution (Embutramide 200 mg + Mebezonium iodide 50 mg + Tetracaine hydrochloride 5 mg), on a dose of 0.5–2 mL according to the animal body weight.

2.4.1. Biochemical analysis

Blood samples were collected under anesthetic conditions, every seven days after the implantation procedure. All blood samples were collected, by the FMV laboratory staff, by jugular venipuncture from the rabbits, between 8:00 and 9:00 a.m. and, before feeding, to avoid diurnal variations. Venous blood samples were collected in the conditions of difficult draws, by using adequate needle and syringe setup, in

order to obtain adequate volumes of the blood samples. Thus, the determination of ionized calcium was done in total venous blood collected into a special 1 mL syringe containing lyophilized lithium heparin. Immediately after collection, the needle was removed, the end of the syringe was cap covered and, the sample was thoroughly mixed for 20–30 s and, then was transferred into Eppendorf tube that was preserved at −80 °C. For all other biochemical markers, after blood collection in a normal syringe, the phlebotomy needle was replaced with a clean needle and, the blood was injected into serum vacutainers containing no anticoagulant. Thirty min after collection, the blood was centrifuged at 3000 rpm for 10 min and the resulting blood serum was rapidly harvested into 2 mL Eppendorf tubes that were stored at −80 °C. The analyses of biochemical markers, (namely, inorganic phosphate (PO_4^{3-}), ionic calcium (Ca^{2+}), alkaline phospatase (ALP) and total proteins (TP)), were performed at the Clinical Biochemical Laboratory (FMV, Iasi, Romania), with an automatic biochemistry analyzer (TCC220) by using clinical biochemistry specific kits (Bio Lab Diagnostics, Mumbai, India).

2.4.2. Histological analysis

The extraction of the bone samples involved a small incision through the skin of the animal to gain access to the external wall of the tibial crest. After removing the implant, the primary bone samples were collected using osteotomes as to contain 1 cm of bone tissue starting from the implant-bone interface and to include the intermediate area of new trabecular bone, bordered by two strips of cortical bone, i.e. the internal bone layer (endosteum) and the external bone layer (periosteum). The primary bone samples were fragmented into thinner pieces (0.3 cm thickness) which were shaped to the final specimens such as to contain the peri-implant capsule and the newly formed bone tissue area (with different ratio woven bone/lamellar bone type of organization), that was formed due to endosteum and periosteum activation and was induced by the bone defect surgery, being directly influenced by the specific effect of the implant in the vicinity of the implant-bone contact area. The final specimens were processed further by fixation (being stored for three days in 10% formaldehyde solution), decalcification (for six weeks, with 15% EDTA solution at pH = 7, and weekly changing of EDTA solution), dehydration (with ascending grades of ethanol solutions, from 96% to 100%), clearing (with xylene), and finally impregnation and embedding (in paraffin). To obtain 5 μm thick bone samples, the cut was performed with a microtome machine. Hematoxylin and Eosin (H&E staining) method allowed the chromatic visualization of the main bone tissue-specific structures, that were examined under an optical microscope by using 4× - 40× magnifications.

Bone histomorphometry is a quantitative assessment of bone microarchitecture able to evaluate bone microscopic organization and structure [30]. It is able to determine bone's microarchitectural parameters (either in 2D, or in 3D -by applying a stereological formula) such as bone area (i.e. the percentage of occupied area by calcified bone in relation to the total tissue area), trabecular width (i.e. the distance across individual trabeculae), and trabecular separation (i.e. the distance between trabeculae). The main histomorphometric structural/static parameters (according to the Nomenclature Committee of the American Society for Bone and Mineral Research, ASBMR) are BV/TV (%) (bone volume/total tissue volume), Tb.Th (μm) (trabecular thickness), and Tb.Sp (μm) (trabecular separation). In our study we have adopted *ImageJ* [31] as freely available software package for image analysis. Recently, van't Hof et al. [32] reported an application of *Java*-based script compatible with freely available open-source *ImageJ* software, that is able to analyze osteoblast and osteoclast activity. Similarly, *BoneJ* is a freely available open-source *ImageJ*-based plugin developed by Doube et al. [33], that allows to achieve standard static/structural bone parameters measurements. In order to determine the above mentioned three parameters, semi-automatic histomorphometry was performed using *ImageJ* and *BoneJ* softwares by selecting the region of interest (2D-ROI) as a circular surface (300 μm diameter) from the intermediate trabecular area corresponding to the new bone formation (located at a distance of 200 μm from the implant) and by applying (for each of the 27 selected ROI surfaces/group) the protocol developed by Doube and coworkers [33].

2.4.3. CT analysis

A high-resolution CT system (X-ray CT, Siemens Somatom Balance, Erlangen, Germany) was used to evaluate the microstructure of each hind limb of the rabbit with implant inserted, with a scanning resolution of 20 μm/slice. 3-D images were reconstructed based on the acquired 2-D image sequences, by using the *Syngo Viewer* image software, Version 2.21.

ImageJ and *BoneJ* softwares were used for semi-automatic evaluation of the three structural bone parameters from CT scans. The corresponding region of interest (ROI) was a 3D parallelepiped-shaped space resulting from adding 1 mm to each main dimension of the implant's contour. In practice, the main stages of the procedure to determine the structural (trabecullar) bone parameters following (for each of the 27 selected ROI surfaces/group) the protocol established by Doube et al. [33] were as it follows, open the image as a virtual stack (by dragging and dropping directory of scan slices onto *ImageJ*), crop the empty slices above and below ROI (with *Plugins → Stacks → Delete Slice Range*), crop the sides (with *ImageJ*'s rectangular region of interest (ROI) tools and *Image → Crop* command), segment automatically into bone and background (with *Plugins → BoneJ →* Optimise Threshold/Threshold only; Apply threshold), measure (BV/TV), bone volume fraction (with *Plugins → BoneJ → Volume Fraction*), measure (Tb.Th) and (Tb.Sp), trabecular thickness and spacing (with *Plugins → BoneJ → Thickness*).

2.4.4. Statistical analysis

Statistical analyses were performed using *IBM SPSS Statistics* (IBM Corp. Released 2012 IBM SPSS Statistics for Windows, Version 21.0; IBM Corp, Armonk, NY, USA) [34]. For in vivo results, Kolmogorov-Smirnov Test of Normality was used in the first stage to evaluate the normal distributions of the result. In the case of biochemical parameters, the statistically significance of the variations registered (statistically significant difference for $p < 0.05$) was verified by Mann-Whitney U Test ($n = 3$), while for histomorphometry and CT bone structural parameters, direct statistical evaluation considered t-test for two independent Means ($n = 27$). Correlations between the variations registered were established by using one-way analysis of variance (ANOVA).

3. Results and discussion

3.1. In vitro electrochemical characterization

In vitro electrochemical testing was performed by exposing samples of the alloys under investigation to naturally aerated Ringer's solution thermostatted at 37 °C. Although Ringer's solution was originally designed as an isotonic solution relative to the body fluids of animals for biological testing, it is often preferred to other simulated body fluids in corrosion studies because the absence of phosphates compared to real physiological solutions leads to the measurement of higher corrosion rates and minimization of corrosion product precipitation [35]. In this way, a non-buffered electrochemical characterization of the corrosion resistance of the material can be attained.

3.1.1. Open circuit potential

The evolution of the open circuit potential (OCP) following immersion in Ringer's solution is shown in Fig. 2. A shift of OCP in the negative direction indicates the activation of metal dissolution in the aqueous environment immediately at short exposure times. At longer times, the shift of the OCP values to more negative potentials occurs at a

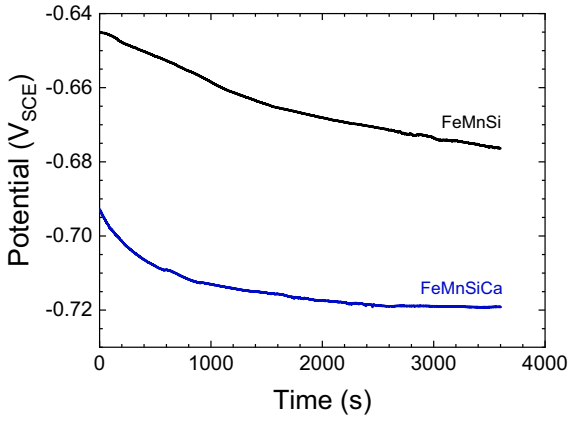

Fig. 2. Initial time variation of the open circuit potential (OCP) for FeMnSi and FeMnSiCa alloys in Ringer's solution at 37 °C.

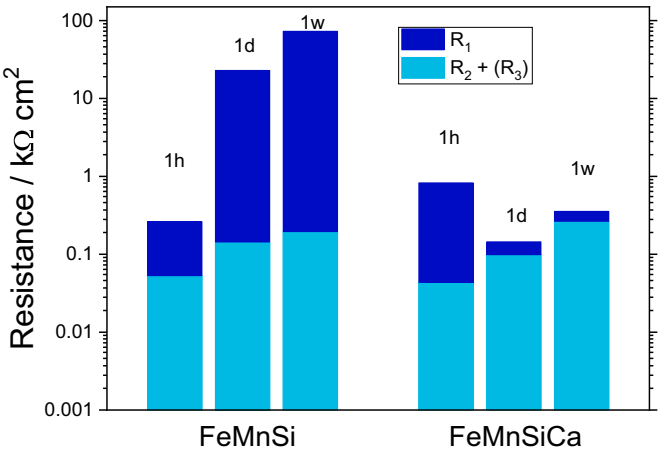

Fig. 4. Time evolution of the total resistance values derived from the fitted impedance data for FeMnSi and FeMnSiCa alloys immersed in Ringer's solution at 37 °C,

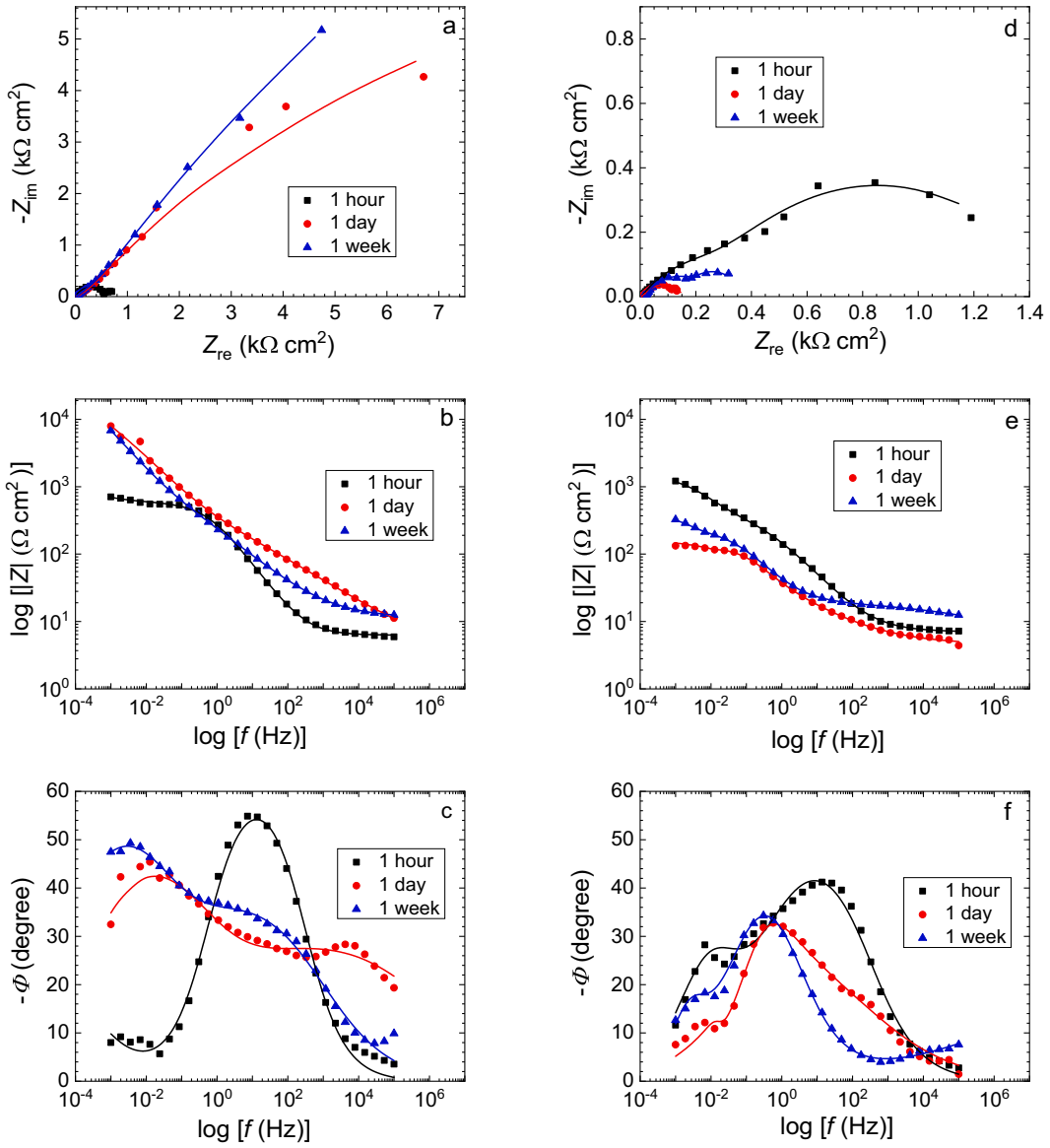

Fig. 3. (a,d) Nyquist plots and (b,e) Bode-amplitude and (c,f) Bode-phase plots recorded for (a–c) FeMnSi and (d–f) FeMnSiCa alloys after different immersion times in Ringer's solution at 37 °C, measured at their corresponding open circuit potential in the electrolyte. Symbols denote the experimental data, whereas the lines give the simulation to the data using an EEC.

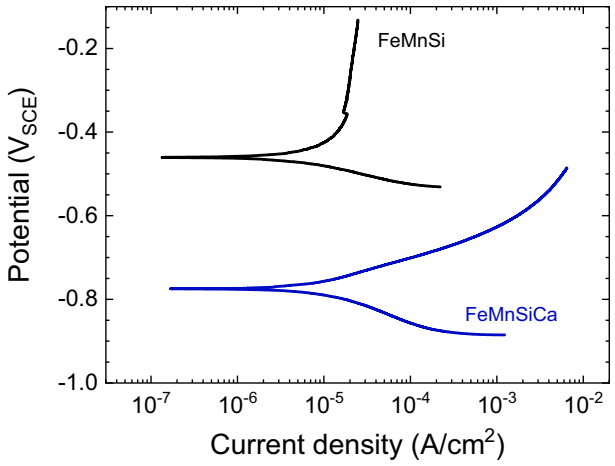

Fig. 5. Linear potentiodynamic polarization plots for FeMnSi and (d–f) FeMnSiCa alloys after 7 days immersion in Ringer's solution at 37 °C. Scan rate: 1 mV/s.

Table 1
Electrochemical parameters determined from linear potentiodynamic polarization tests for FeMnSi and FeMnSiCa samples immersed for 7 days in Ringer's solution at 37 °C.

Material	OCP (V_{SCE})	j_{cor} (mA/cm^2)
FeMnSi	−0.462	3.37
FeMnSiCa	−0.773	8.44

slower rate, indicating an almost stationary regime. Therefore, electrochemical tests were initiated after 1 h exposure to the simulated body fluid. As it can be seen in Fig. 2, the OCP of the FeMnSi alloy shifted to the negative direction of potential with the addition of Ca, by approximately 50 mV, probing the latter to be a more electrochemically active material towards corrosion.

3.1.2. EIS measurements and equivalent circuit analysis

EIS measurements were performed after 1 h, 1 day and 1 week of immersion in Ringer's solution, producing the impedance plots presented in Fig. 3 for the FeMnSi and the FeMnSiCa alloys. Impedance data are displayed as both Nyquist (real vs. minus the imaginary part of the impedance), and Bode-amplitude and Bode-phase diagrams (modulus ($|Z|$) and phase angle (Φ) vs. frequency (f), respectively). Analysis of the electrochemical impedance data was performed by fitting an equivalent circuit (EEC) that provided the best correlation between experimental and fitted data while leading to χ^2 values in the 10^{-3} to 10^{-4} range. The capacitive components were better described using a constant phase element, Q, instead of a pure capacitance, whose impedance is determined using [36]:

$$Z_Q = (j\omega)^{-n}Q^{-1} \quad (1)$$

where n may vary from 0 (pure resistance) to 1 (pure capacitor), in which case Q would be equal to the capacity of the capacitor; ω is the angular frequency; and j is the imaginary number ($j^2 = -1$). In addition, a resistance component R_s representing the resistance of the solution was introduced in the EEC although it does not depend on the substrate surface.

The FeMnSi and FeMnSiCa alloys immersed in Ringer's solution initially behaved as a bare metal exposed to the electrolyte, and the EIS data could be satisfactorily described by the classical Randles-Ershler equivalent circuit [37], which contains a double layer capacitive element in parallel with the charge transfer resistance and a diffusive impedance in the electrolytic phase given by the Warburg impedance. But the development of an oxy-hydroxide layer soon coexisted with metal dissolution due to corrosion, and the physicochemical system was then described using two-time constants (i.e., two combinations in parallel of a resistor and a pseudo-capacitor). The two-time constants could be easily distinguished from the Bode-phase plot already as early as 1 h immersion for the FeMnSiCa alloy. This feature reflects the presence of two interfaces, namely metal oxide-electrolyte and metal-electrolyte, represented by the R_1Q_1 and R_2Q_2 pairs of elements, respectively [38]. That is, the oxy-hydroxide layer formed on the alloy presented pores and defects that allowed the aggressive species present in the electrolyte to reach the metal surface. The constant phase elements of the metal oxides and at the reacting metal surface have an intermediate behaviour between those corresponding to a capacitor and a resistor, as evidenced by n values close to 0.5. This reflects the presence of a leaking double layer which, according to the Q values, progressively increases in capacitance upon exposure to the electrolyte. At the same time, the metal-metal oxide interface accounts for a larger resistance to the charge transfer process and more capacitive behaviour. Inspection of the impedance spectra recorded for the FeMnSiCa alloys shows the onset of a third time constant that could be distinguished in the low frequency range for the impedance spectrum measured after 1-day exposure. Although this third time constant could not be resolved using the fitting software in this case, the divergence between the experimental and the fitted data is observable at the low frequency limit in Fig. 3d–f. At longer exposures, the new time constant could be satisfactorily modelled for the impedance spectrum recorded after 1 week. The new time constant arose from the accumulation of ionic species in the electrolyte volume adjacent to the fast corroding surface, leading to the precipitation of a new layer formed by corrosion products inside the pores and defects developed in the non-sealing oxy-hydroxide layer.

Further inspection of the spectra depicted in Fig. 3 allows distinguishing a major difference in regards to the time evolution of the system. That is, the corrosion activity of the FeMnSi decreases abruptly upon immersion in the electrolyte due to passivation of the surface by the formation of an oxy-hydroxide layer sufficient to slow down the metal dissolution rate from the alloy, resulting in 10-fold increase of the impedance modulus in the low frequency range as observed in Fig. 3b, layer that was already developed after 1-day exposure, whereas it aged slowly for longer exposures (see Fig. 3a and b). Nevertheless, the layer formed on the surface of the alloy was not an efficient dielectric barrier layer because it was unable to attain a frequency range with capacitive behaviour in the Bode-phase diagrams shown in Fig. 3c, but its resistance was sufficient to provide some degree of passivation to this alloy in the test electrolyte.

In the case of the alloy containing Ca, the EIS diagrams depicted in Fig. 3d–f clearly show a trend to decrease the sample impedance shortly after exposure to the test electrolyte, that is observed from the reduction of the diameter of the semicircle in the Nyquist plot (cf. Fig. 3d), and from the decrease of the impedance values in the Bode plot in the low frequency range (Fig. 3e). Thus, impedance data show a progressive activation of the sample during immersion in Ringer's solution, thereby accelerating the corrosion rate when exposed to this simulated body fluid. In fact, the slower corrosion rates for the Ca-modified alloy were observed only at the beginning of the experiment (cf. Fig. 3d), when the corrosion rate was close to that exhibited by FeMnSi (Fig. 3a). In addition, the decrease of the electrochemical impedance for longer exposures mainly occurred in the low frequency range, which accounts for the electrochemical characteristics of the oxy-hydroxide layer developed on the metal. Although slightly higher values for the impedance modulus in the low frequency range were registered after 1-week exposure to the physiological solution, this effect was accompanied by the observation of higher dissolution rates at the metal-metal oxide interface in the high frequency range. This feature supports that although some precipitation process may also occur on FeMnSiCa sample at longer exposures, it is insufficient to hinder metal dissolution. Therefore, in vitro electrochemical characterization is consistent with a

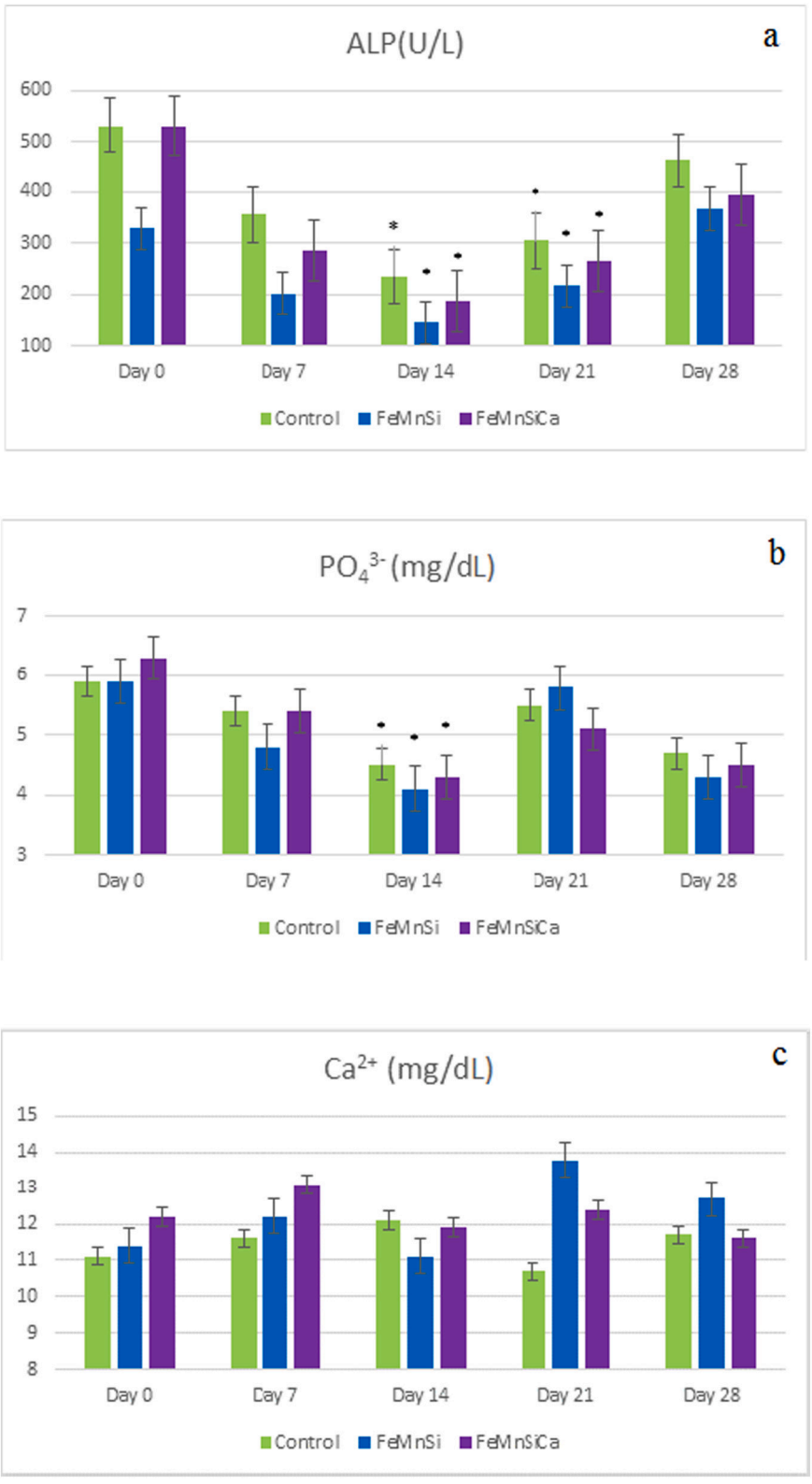

Fig. 6. Dynamics of blood serum mean values of (a) inorganic phosphate, (b) alkaline phosphatase activity, and (c) total calcium during the rabbit experimental model with tibial implant. *Statistically significant difference ($p < 0.05$) when compared to day 0.

more biodegradable material than the FeMnSi alloy considered as reference.

It is also important to observe that the total resistance of the FeMnSiCa alloy is more than one order of magnitude smaller than for the FeMnSi alloy at the end of the in vitro tests (e.g., 0.597 and 45.7 kΩ cm^2, respectively). More interestingly, the inspection of Fig. 4 leads to observe that the R_2 component accounts totally for the observed change in the total resistance. This fact indicates that the addition of Ca to the FeMnSi alloy, although as minor constituent, is very effective in preventing or at least reducing the growth of the oxy-hydroxide layer on

Control	FeMnSi	FeMnSiCa
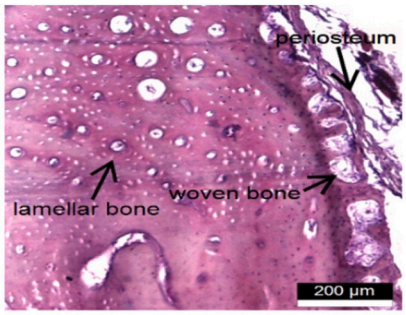 a	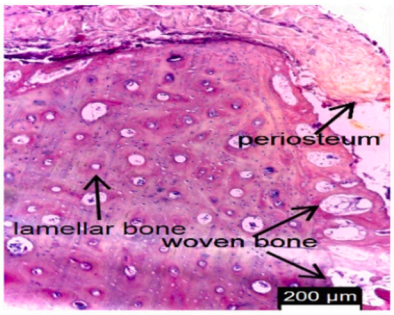 b	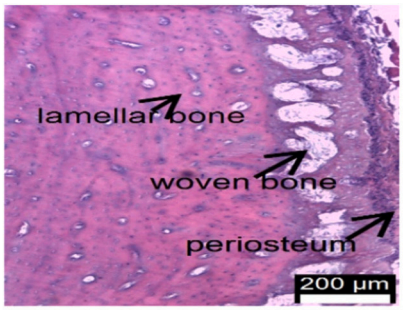 c
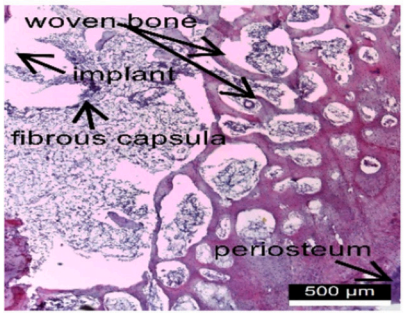 d	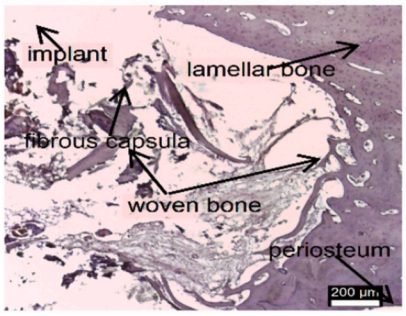 e	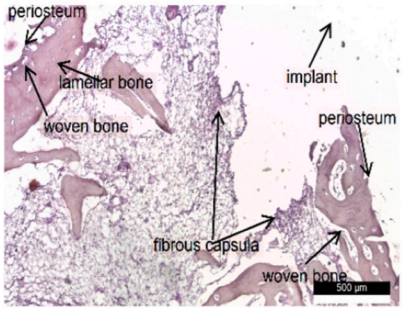 f
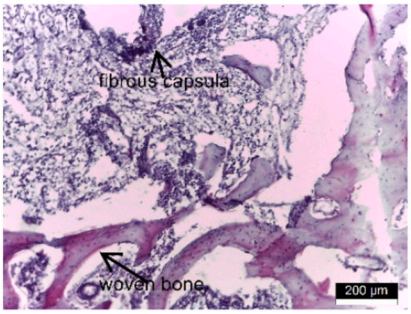 g	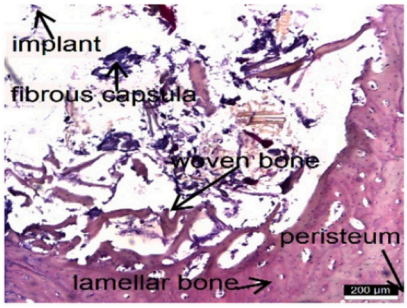 h	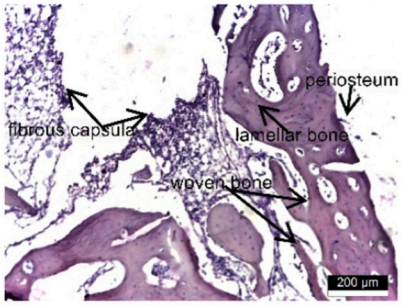 i
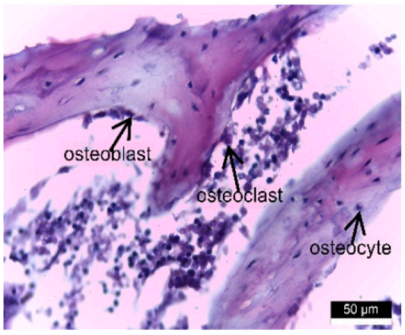 j	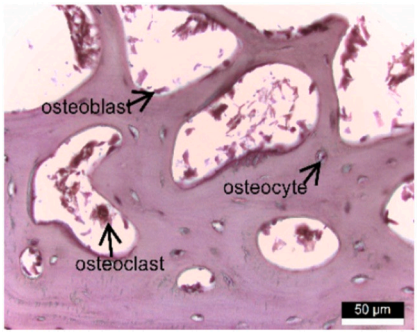 k	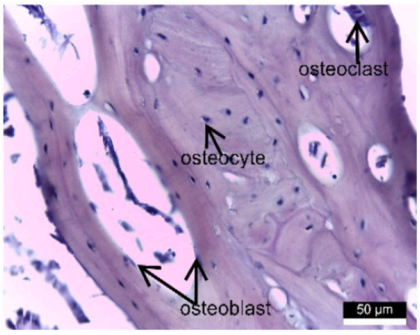 l

(caption on next page)

Fig. 7. Morphology of bone tissue at the implant-bone interface of the three experimental rabbit groups (Control, FeMnSi and FeMnSiCa): a) after 2 weeks (first row) and b) after 4 weeks (second row) from implantation surgery with details presenting b1) new woven bone/lamellar bone ratio (third row) and predominance of the main cell types of bone tissue (fourth row). Coloration HE ×500, ×200, ×50.

Table 2
New woven bone structural parameters according to *BoneJ* histomorphometry of H&E stained histological samples from rabbit's tibia at 2 and 4 weeks post-implantation.

Parameter	Group					
	Control		FeMnSi		FeMnSiCa	
	@ 2 weeks post-implantation	@ 4 weeks post-implantation	@ 2 weeks post-implantation	@ 4 weeks post-implantation	@ 2 weeks post-implantation	@ 4 weeks post-implantation
BV/TV (%)	30.05 ± 4.65	46.15 ± 5.12	39.42 ± 3.19	49.97 ± 4.72	54.82 ± 5.79*	68.12 ± 6.81*
Tb.Th (μm)	23.63 ± 3.23	28.97 ± 3.73	24.77 ± 3.43	30.37 ± 4.16	27.96 ± 3.05	37.35 ± 3.63*
Tb. Sp (μm)	25.55 ± 3.53	21.12 ± 3.25	21.25 ± 2.63	17.12 ± 2.03	17.54 ± 1.64*	13.33 ± 1.65*

* Statistically significant difference ($p < 0.05$) when compared with the control group ($n = 27$).

Table 3
Surface topography characterization of the samples removed from animal testing for 28 days and subsequent cleaning.

Material	Specific surface of pores (3D)	Porosity (%)	Average roughness, R_a (μm)
FeMnSi	0.014	0.601	6.801
FeMnSiCa	0.028	0.758	4.944

the corroding metal in Ringer's solution, thus hindering its passivation.

3.1.3. Potentiodynamic curves

Linear polarization measurements were performed at the end of the in vitro tests, immediately after recording the EIS spectra for 1-week exposure. The corresponding Tafel plots are given in Fig. 5 depicted as semi-logarithmic diagrams, and the relevant electrochemical parameters derived from their analysis are listed in Table 1. The behaviour of the two alloys differed significantly after 7-day immersion, leading to a more positive OCP value only in the case of the base FeMnSi alloy, which is an indication of the development of an oxy-hydroxide layer on the surface of this material. Conversely, the OCP value determined for the FeMnSiCa alloy is slightly more negative than the value attained at the beginning of the experiments (cf. Fig. 2). This is an indication of the inability of the modified alloy to achieve a passive condition. Although the corrosion current densities obtained from the corresponding Tafel lines are similar for both metals, a current plateau (characteristic of the passivation process) could be found in the anodic branch for the FeMnSi alloy, which supports a bigger degradation rate for the alloy modified by adding 1 wt.% Ca.

3.2. Evaluation of in vivo osseointegration

3.2.1. Dynamics of total calcium, inorganic phosphate and alkaline phosphatase activity mean values from the rabbit experimental model with tibial implant

In the growing rabbits, the high-serum alkaline phosphatase activity is determined by the physiological skeletal growth and is positively related to the intense osteoblastic activity able to assure a fast recovery of bone defects when needed [39–42]. Moreover, our previous experiments with bone implants inserted in young growing animals [15–17,19,41,42] support observations from other studies that sustain a high potential of blood alkaline phosphatase's activity as a real valuable diagnostic indicator of metabolic transformations involved in the bone recovery process [43]. In the case of the young rabbits with tibial implant, the alkaline phosphatase activity registered statistically significant variations ($p < 0.05$) at 7, 14 and 21 days (see Fig. 6a), and statistically insignificant variations at 28 day post implantation for all experimental groups, when compared with the normal state before surgery (day 0). Following other relevant studies [37,44–54], these observations signal a proper evolution of various metabolic processes generated by the significant activation of osteoblasts (with the subsequent increase of the alkaline phosphatase activity) for the period between 7 and 21 days post-implantation, that was able to ensure a bone recovery state close to normal at the 28th day.

The fluctuations of inorganic phosphatemia (cf. Fig. 6b) and blood ionic calcium (Fig. 6c), two general clinical biochemical parameters that are most intrinsically associated with alkaline phosphatase activity and bone recovery process [55,56], cannot be explained directly by the primary cause-effect algorithms, given the interference of many others various individual reactive factors that are able to modify the protective influence of the body's (buffer) capacity to ensure homeostasis, either locally (i.e., at the bone tissue level) or generally (i.e., at the blood level). However, statistical correlations (Anova test) between these two biochemical markers and alkaline phosphatase activity allowed a general summative (and associative) interpretation of the involvement's degree of various local/cellular metabolic processes in the repair of bone defects. Thus, although the values of inorganic phosphatemia and alkaline phosphatase activity recorded on day 7 post-implantation registered statistically non-significant ($p > 0.05$) low variations (when compared with the normal state before surgery, day 0), on the 14-day post-implantation the variations recorded were statistically significantly lower ($p < 0.05$), which may be considered as a delayed metabolic disturbance induced by the surgical trauma, that normally is reported to occur in the first seven days post-implantation [57–64]. In addition, the statistically significant increase ($p < 0.05$) of inorganic phosphate value registered in the day 21 as compared to the 14-day post-implantation was only moderately correlated ($R^2 = 0.523$) with the increased activity of alkaline phosphatase, being most probably a lately effect induced by the osteoblasts' activation and the subsequent intense woven bone formation, according to the conclusion of other interdisciplinary reports [15,19,41–46,55–59]. Next, the statistically non-significant hypophosphatemia ($p > 0.05$) recorded between 21 and 28 days was strongly correlated ($R^2 = 0.973$) with the statistically non-significant hypocalcemia ($p > 0.05$), and this was explained on the basis of other relevant studies [48–53] by considering the transformation of the osteoblasts into osteoclasts once stabilization of its osseous structure will be initiated with their entrapment by the extracellular matrix of calcium phosphate and will subsequently intensify the osteoclasts' activation in order to assure the evolution of the woven bone into lamellar bone.

3.2.2. Histological evaluation of the bone-implant interface

No inflammatory effects or signs of rejection were observed [60–62] for any histological bone sample from any of the three groups of rabbits.

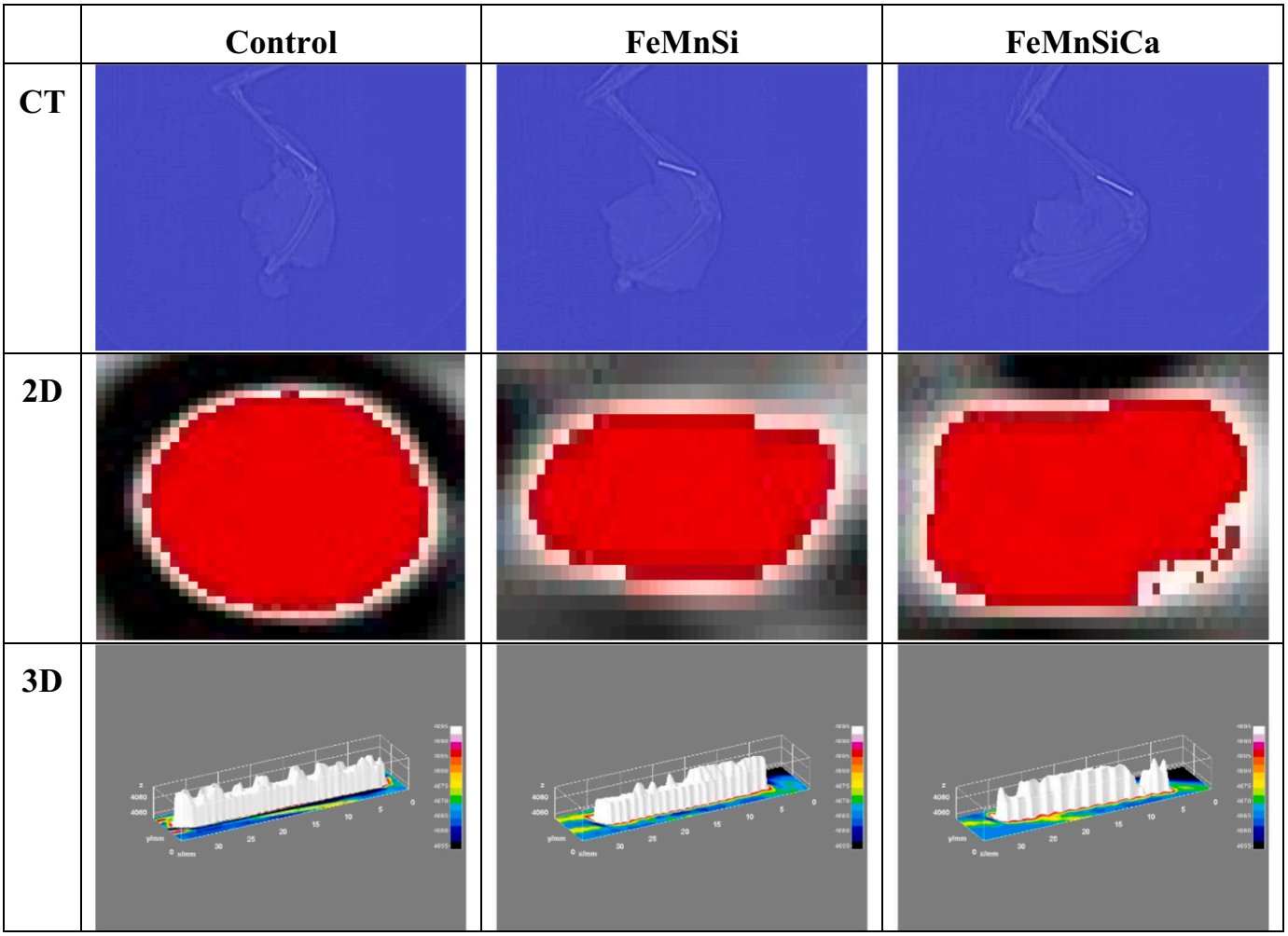

Fig. 8. CT scans (showing implant insertion in the rabbit's tibia crest), 2D reconstructed transversal section through implant (red color for alloy's intrinsic structure and white color for the newly formed/deposited bone tissue) and 3D reconstructed images of the implanted specimens in rabbit tibia (showing % of new bone tissue (woven bone) formed on the whole implant's surface and on its close 3D vicinity). (For interpretation of the references to color in this figure legend, the reader is referred to the web version of this article.)

In the histological images presenting the bone tissue morphology at the implant-bone with defect interface, after 2 weeks from implantation surgery (Coloration HE ×200, Fig. 7a), an intense cell multiplication of osteoprogenitor cells, massive proliferation of the fibrosis layer of the periosteum, and a significant formation of woven bone as well as a small amount of lamellar bone may be observed, similarly to data reported by other studies [60–66]. Additionally, a simple visual comparison of the three experimental groups (namely, Control, FeMnSi and FeMnSiCa) highlighting a bigger proliferation of the woven bone and, an initial somehow increased proportion of lamellar bone, in the case of FeMnSiCa group, medium for the FeMnSi group and lowest for the control group, is also sustained by the results of bone structural parameters (evaluated histomorphometrically with *BoneJ* software) that are presented in Table 2. Moreover, the greater number of active and bigger osteoblasts, with many large extensions, arranged on multiple rows, induced by the proliferative differentiation tissue present in the thickened periosteum as well as in the areolas and in immature bays highlights a bigger osteo-induction process with a subsequent greater regeneration of the bone with defect tissue, as woven bone [64] in the case of the FeMnSiCa group.

In the histological images (Coloration HE ×500) presenting the bone tissue morphology at the implant-bone with defect interface, after 4 weeks from implantation surgery (see Fig. 7b), may be observed that on a normal background of the periosteum thickness, with no more hypercellularity, the amount of lamellar bone (showing darker ossification lines) start to increase, even the woven bone is yet abundant in the adjacent area to the obliquely disposed implant. A detailed image (Coloration HE ×200) that compares the ratio of woven bone/lamellar bone (shown in Fig. 7c) for the three experimental groups (namely, Control, FeMnSi and FeMnSiCa) evidences the exceeded proportion of the lamellar bone (evolved from the woven bone-yet abundant in the implant's adjacent area), that was higher in the case of FeMnSiCa group, medium for the FeMnSi group and lowest for the control group. Additional details (Coloration HE ×50) presenting the main type of bone cells attached to the bone trabeculae (see Fig. 7d), outlines a normal proportion of osteoblasts and only few/rare osteoclasts, but also the presence of a large number of active osteocytes in the case of FeMnSiCa group, as compared with the medium number in the case of FeMnSi and low number in the control group. These observations are sustained by the values of the main structural parameters listed in Table 3, that are specific to the bone histomorphometry, performed with *ImageJ* and *BoneJ* softwares, by selecting ROI (300 μm circular surface) from the intermediate (trabecular) new bone area. Under the general limitations imposed by the tissue disruption, occurring when bone samples are harvested (fact affecting preservation of the structure closer to its in vivo appearance) bone histomorphometry allowed to achieve information from the insight of the new (formed) bone (tissue) organization for all three experimental groups. Thus, in the implant-bone with

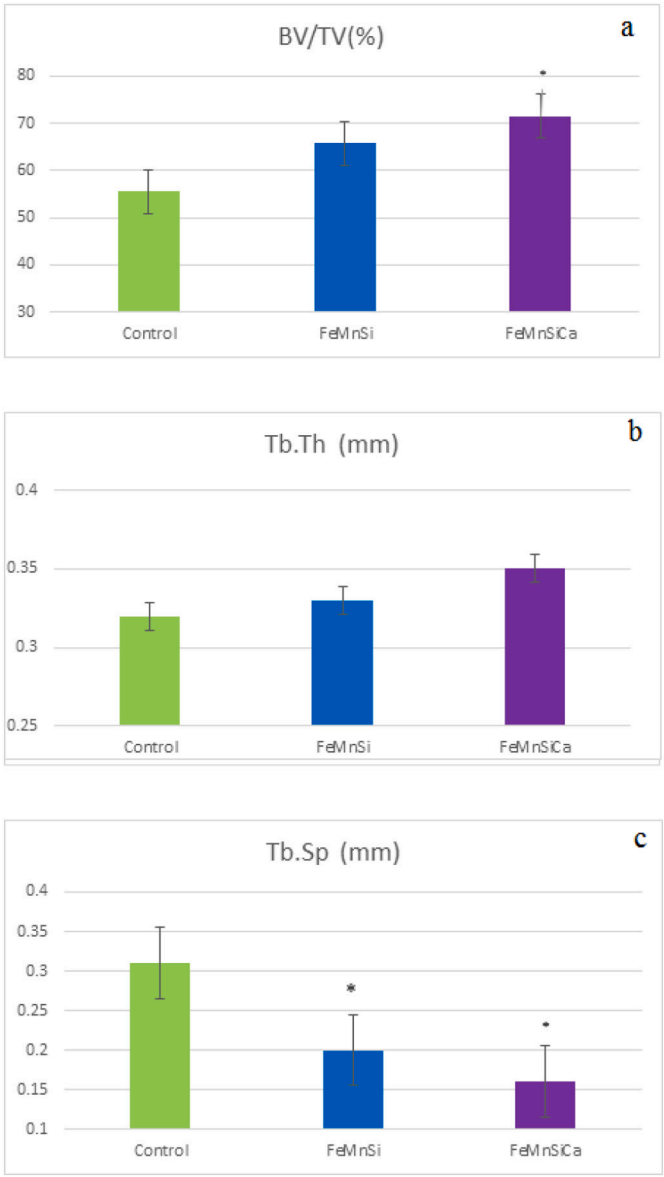

Fig. 9. Main structural parameters (BV/TV, Tb.Th, and Tb.Sp mean) of the new bone formed on the implant's surface according to BoneJ processed CT scans in rabbit's tibia at 4 weeks post-implantation.

defect vicinity, on the background of statistic significant ($p < 0.05$) higher ratio (%) of new woven bone volume per total tissue volume, the trabecular thickness (Tb.Th.) registered statistically significant higher values, while the spaces between the trabeculae (Tb.Sp.) showed statistically significant decreased values ($p < 0.05$), a fact sustaining that higher osteoinductive capacity and an evolved degree of osteoconduction process occurred in the case of the FeMnSiCa group compared to either FeMnSi or the control groups.

3.2.3. CT characterization

Bone's microarchitecture and microstructure testing of the reconstructed images resulted through computed tomographic analysis, started lately to gain a leadership position even in the case of selected CT scans, (similarly as in the case of selected bone histomorphometry images), still prevails the practical need to establish an optimized standardized algorithm for preventing any interference with the quantification procedure during analysis [30,65–68].

The computed tomography investigation allowed to evaluate the integrity of the implant's cross-sectional surface/shape but also the microstructure of the newly formed bone tissue deposited on the surface of the implant, as a measure of various processes involved in the repair of the bone defect [15,19],

Thus, the reconstructed 2D images of the implant's (transversal section) surfaces given in Fig. 8 showed that, the integrity of the implant's (most) central cross-sectional surface/shape (red colored) was affected by the biodegradation process (when compared to control) in a bigger proportion in the case of the FeMnSiCa implant and in a medium proportion for the FeMnSi implant, in good agreement with the corrosion test's results from Section 3.1.1.

Also, the reconstructed 3D images of the new bone tissue deposited on the implant surface (Fig. 8) highlighted that one month after the implantation surgery, the FeMnSiCa implant was covered in greater proportion with a thick layer of the newly formed bone. Thus, the ratio (%) of the new bone volume per total tissue volume as shown in Fig. 9, was highest in the case of FeMnSiCa group, being statistically significant ($p < 0.05$) when compared with the control group. Moreover, even the value of trabecular thickness (Tb.Th.) showed the highest values in the case of the new trabecular bone tissue deposited on the FeMnSiCa implant surface, without registering statistically significant differences ($p > 0.05$) for any of the experimental groups, the statistically significant decreased values ($p < 0.05$) of the trabecular spaces (Tb.Sp.) revealed a more advanced organization, according to other relevant studies [59–62], of the new bone tissue deposited on the surface of FeMnSiCa, in comparison with the control group, fact induced by the higher osteoinductive and osteoconductive capacity of FeMnSiCa implant.

3.3. Surface characterization of the implanted specimens

Fig. 10a–b shows the morphology of the alloy (i.e. (a) FeMnSi and (b) FeMnSiCa) surfaces, per se harvested after implantation while Fig. 10c–d of the alloys (i.e. (c) FeMnSi and (d) FeMnSiCa) after subsequent cleaning by ultrasonication.

Image analysis of the just harvested samples revealed the formation of consistent deposits on the surfaces of both samples during the implantation period, and such a deposition process was more extensive on the FeMnSiCa sample. According to our previous report [15], on the surface of the implanted specimen will initially appear Fe, Mn, Si, Ca and Mg oxides, which will form hydroxides when interacting with the internal hydrophilic environment of the body. In addition, these oxy-hydroxides can further react with various ionic components of the blood or bone tissue to form salts, which either will be taken up and transported by the blood to other tissues, or once the nucleation centers are induced, will be deposited on the surface of the implant together with the other salts of Na, Mg, or Ca and P. The ratio between the stability and the reactivity of the resulting oxy-hydroxides and salts will influence the intensity of the biodegradation processes and the type of corrosion manifested by the implanted alloy in the bone tissue [1,2].

The present experiment on rabbits strengthens the conclusions of our previous in vivo investigation on Wistar rats [15] that showed a very good bio-compatibility of the FeMnSi subcutaneous implant due to the absence of any kind of local reaction or toxic systemic fact, which was explained in terms of the slow degradation of the alloy and the consequent metabolization of the resulted byproducts without perturbing the body's homeostasis. Moreover, the FeMnSi alloy implanted in the rat (tibiae) model, did not induce any adverse biological reaction and provided temporary mechanical support to the affected bone area. Similarly, the implantation of FeMnSi and FeMnSiCa alloys, in the rabbit's tibia, generated various Fe, Mn and Si oxides/hydroxides as the main significant biodegradation or corrosion by-products and, a major quantity of phosphorus and calcium derivatives, formed as a result of the interactions with HPO_4^{2-} and Ca^{2+} ions mobilized from the blood, disposed in bigger proportion in the case of FeMnSiCa (compared to FeMnSi) in overlapping layers to the alloy's surface.

The cleaning by ultrasonication of the implanted samples revealed a

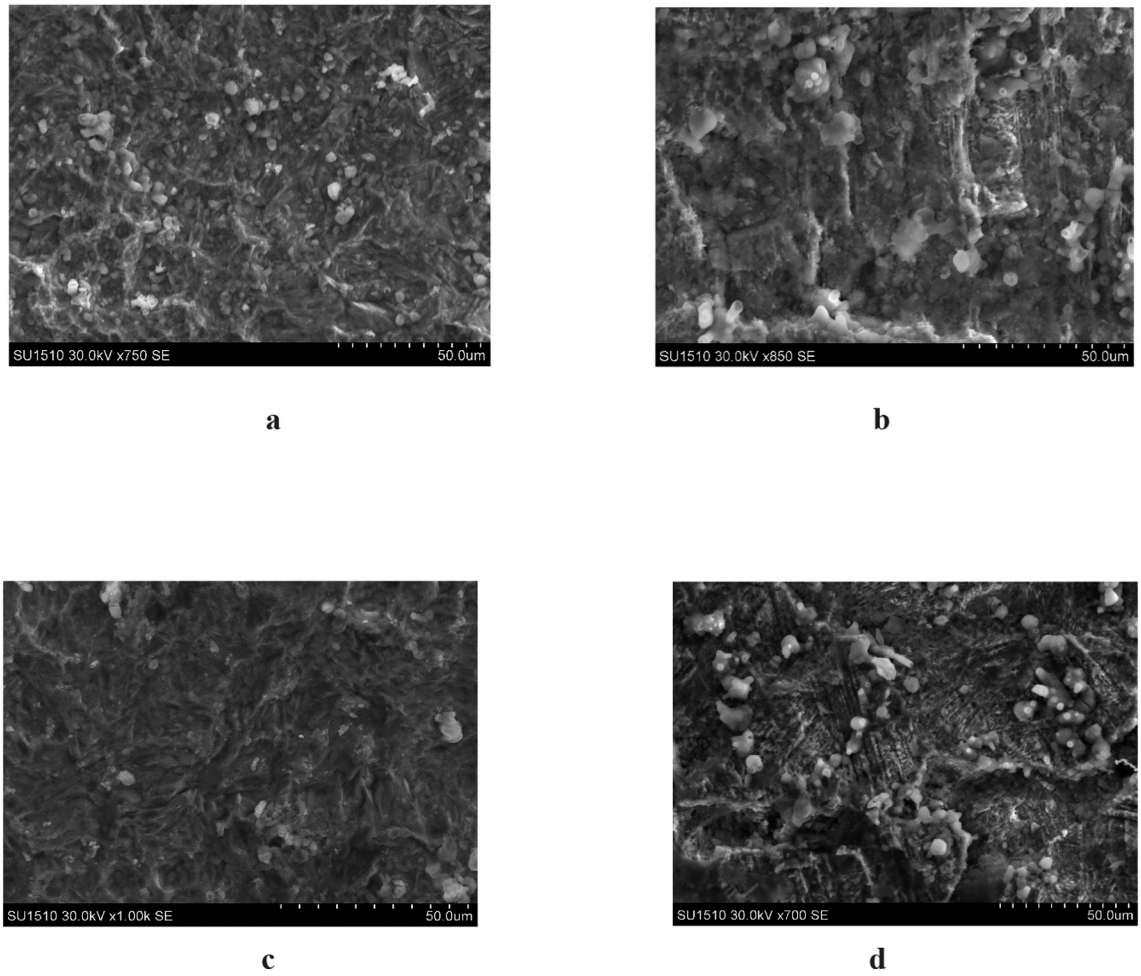

Fig. 10. SEM micrographs of (a) FeMnSi and (b) FeMnSiCa specimens as harvested from the animal models after the in vivo tests, and of (c) FeMnSi and (d) FeMnSiCa specimens following subsequent ultrasonic cleaning of the harvested sample from the animal models after the in vivo tests. *Statistically significant difference ($p < 0.05$) when compared to day 0.

larger fraction of the surface area affected by general corrosion in the case of the FeMnSiCa sample (see Fig. 10d) than for the master FeMnSi alloy (Fig. 10c). This feature probes that Ca addition induced an increased reactivity of the FeMnSiCa alloy by enhancing interactions at the bone-implant interface. A detailed analysis of the surface topography indicates that on the background of an average roughness, the denser closely spaced irregularities (shown by the plot surface profiles included in Fig. 11c–d), are the main indicators that highlight the increase in surface biodegradability through increased reactivity induced by the addition of Ca in the FeMnSiCa alloy. Further analysis of the 2D- and 3D-reconstructed SEM images allowed porosity evaluations to be conducted along the red lines drawn on the micrographs of Fig. 11c–d [69,70]. Although porosity data obtained in this way maybe regarded less precise than those obtained from AFM measurements, they can be employed for the sake of comparison of the final surfaces of the retrieved implants, and the obtained data are summarized in Table 3. Larger values for the 3D specific surface pores and porosity were found for the FeMnSiCa specimen (cf. Fig. 11e–f), a feature that can be regarded as a major sign of an extensive general corrosion of FeMnSiCa alloy.

Given that the initial thickness of the FeMnSi implant was 500 μm, while the remaining thickness after extraction and ultrasonic cleaning of the implant was 490 μm (determined as the average of three separate measurements), then around 10 μm of metallic material was lost during the implantation period. By considering that degradation rates should be approximately the same at each end of the sample, we can consider that 5 μm were lost from each side. Analogously, the variation of the thickness of the FeMnSiCa implant as a result of the implantation process can be determined by comparing the initial value of 450 μm with that observed after extraction and ultrasonic cleaning as being 400 μm (average of three measurements). Thus, approximately 50 μm of metallic material was lost during implantation period, with 25 μm for each side. Assuming an ideal constant degradation rate to operate during the implantation period, complete degradation of the implanted samples would require 50 months for the FeMnSi implant and only 9 months for the FeMnSiCa implant. Although the complexity of the degradation process would require further elaborated analyses [71–73] to establish the actual period of time needed for the degradation process of both specimens, a rough estimate of ca. 6-fold higher degradation rates for the Ca-containing alloy can be estimated. This estimate correlates very well with the 1-order of magnitude increase derived from the in vitro corrosion tests as described in Section 3.1.2.

The retrieved specimens were further analyzed by EDS to monitor changes in the composition distribution of the main constituent elements of the alloys over the implantation period. For the sake of reproducibility, EDS analysis was performed at three representative locations over the investigated surfaces, and the main observations are listed in Tables 4 and 5 for FeMnSi and the FeMnSiCa alloys, respectively. Thus, the first three areas represented the corresponding surfaces of the FeMnSi and the FeMnSiCa specimens after implantation, while the last three areas corresponded to the same specimens after implantation and cleaning. It is interesting to observe that the same

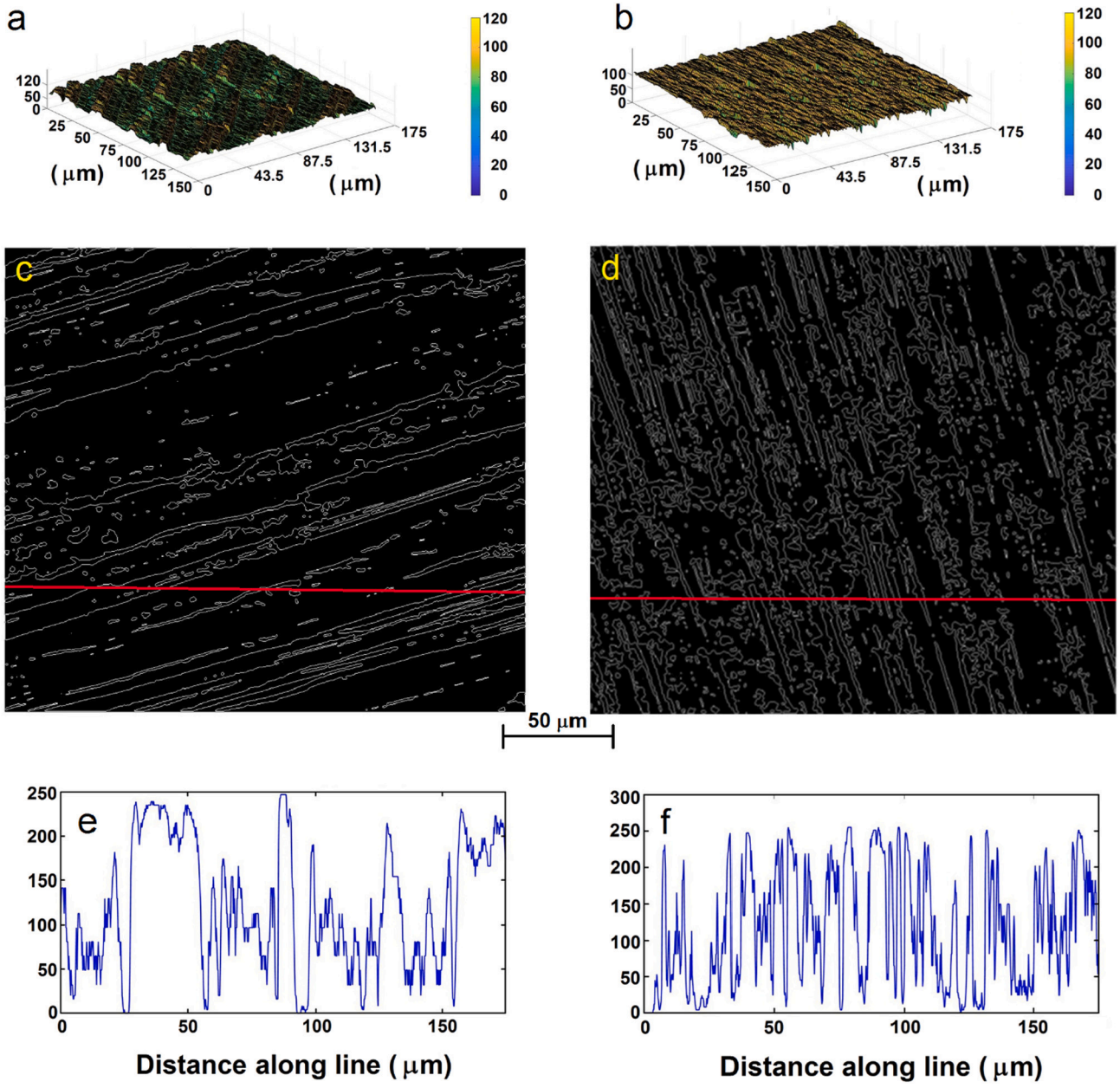

Fig. 11. Surface topography analysis for SEM micrographs of (a,c,e) FeMnSi and (b,d,f) FeMnSiCa specimens after implantation and following subsequent ultrasonic cleaning.

Table 4
Surface composition by EDS from a FeMnSi specimen after implantation (areas 1–3), and after implantation and cleaning (areas 4–6). See the text for details.

FeMnSi alloy	Element								
	Fe (wt.%)	Mn (wt.%)	Si (wt.%)	O (wt.%)	Ca (wt.%)	P (wt.%)	K (wt.%)	S (wt.%)	C (wt.%)
Area 1	41.00	0.34	0.66	10.54	7.14	9.89	1.21	1.63	27.59
Area 2	27.96	0.25	0.54	18.07	13.88	12.82	1.42	1.78	23.28
Area 3	44.28	0.35	0.73	10.77	9.32	10.63	1.52	1.58	20.83
Area 4	85.97	10.53	1.29	2.21	–	–	–	–	–
Area 5	83.98	12.55	1.06	2.41	–	–	–	–	–
Area 6	82.74	13.67	1.25	2.34	–	–	–	–	–

Standard deviations: Fe: ± 1.1; Mn: ± 0.22; Si: ± 0.3; Mg: ± 0.1; Ca: ± 0.05.

Table 5
Surface composition by EDS from a FeMnSiCa specimen after implantation (areas 1–3), and after implantation and cleaning (areas 4–6). See the text for details.

FeMnSiCa alloy	Element								
	Fe (wt.%)	Mn (wt.%)	Si (wt.%)	O (wt.%)	Ca (wt.%)	P (wt.%)	K (wt.%)	S (wt.%)	C (wt.%)
Area 1	29.79	2.36	0.12	14.68	6.86	9.82	1.14	–	35.23
Area 2	30.71	1.92	0.08	14.59	6.16	7.76	1.30	1.66	35.83
Area 3	52.18	5.55	1.42	7.69	4.82	7.26	0.76	1.22	19.11
Area 4	83.27	10.77	3.58	2.37	–	–	–	–	–
Area 5	81.78	12.70	3.39	2.13	–	–	–	–	–
Area 6	81.01	13.37	3.40	2.21	–	–	–	–	–

Standard deviations: Fe: ± 1.1; Mn: ± 0.22; Si: ± 0.3; Mg: ± 0.1; Ca: ± 0.05.

specific signals were observed for both specimens either as retrieved or after ultrasonic cleaning: two energy lines for Fe (with k_a peak being much bigger then k_b peak), two energy lines for Mn (with k_b peak being much bigger then k_a peak), and one energy line for Si. The major difference aimed the Mn peak (k_a), which was more intense and shifted to lower Energy-keV values in the case of the FeMnSiCa specimen. The lack of Ca signal from the implanted specimen after ultrasonic cleaning reveals that calcium was quantitatively lost from the metallic material surface. This feature can be attributed to the transformation of calcium from the alloy surface into ionic calcium (Ca^{2+}) in the hydrophilic environment of the internal body. These ionic species will subsequently diffuse from the corrosion layer, being able to react with $(PO_4)^{3-}$ or $(CO_3)^{2-}$ anions from the blood/bone tissue in order to form calcium phosphate and carbonate salts [15].

Both implanted specimens, prior to ultrasonic cleaning (see areas 1–3 in Tables 4 and 5) showed rather high quantities of oxides, as well as C and Ca-P based compounds, but also some K and S derivatives occurred, either being new species formed and deposited on the metallic surface, or biological tissue traces. After ultrasonic cleaning of both implanted specimens, the areas 4–6 showed that large quantities of Si oxides, some amounts of Fe and Mn oxides together with C-based compounds as well as various salts were removed. Thus, more than 80% of the deposited compounds were detached from the surface, such that, only in some areas, it remained some stable oxides and small quantities of calcium-phosphorus based compounds. The Mn percentage close to the initial values and the higher quantity of Si from the specimens cleaned by ultrasonication (i.e., areas 4–6) may be explained (in good accordance with the kinetics of Si oxides formation and with the passing rates of Fe, Mn, and Si compounds into solution), by the continuous transfer of the oxides of these elements into the hydrophilic environment of the internal body, either being blood or bone tissue. These results outline that Mn compounds from the implanted alloy are more prone to corrosion than Si compounds due to their higher electrochemical potential that will induce an increased reactivity. In order to preserve the shape memory properties of the FeMnSi specimen [74–76], the added content of Ca in the alloy was kept very low (under 1 wt.%). After implantation, the low Ca concentration was reduced even more, due to its bigger reactivity in the bone tissue environment. Thus, the EDS investigation of the implanted and cleaned sample showing no signal for Ca (that was below the detection limit of 0.05 wt.%) is in agreement with previous reports describing the role of calcium addition for increasing the degradation rate of the FeMnSi alloy [16,23,77].

Additionally, the differences in concentration between areas 1 and 2 (cf. Tables 4 and 5) outlined the heterogeneous composition of the degradation layers developed on the surface of the alloy. In the case of area 3, the oxide layer was not compact, thus leading to the observation of larger signals for the main element constituents (Fe,Mn,Si) of the alloy.

4. Conclusions

In vitro electrochemical testing of FeMnSi and FeMnSiCa alloys in Ringer's solution showed more than one order of magnitude decrease of the total resistance of the material for the Ca-containing alloy.

In vivo testing of the alloys in a rabbit's tibia model for 28 days evidenced higher osteoinductive and osteoconductive capacities of the FeMnSiCa implant on the basis of bone histomorphometry and CT tests. Retrieved implants showed generalized corrosion on their surfaces, although to a larger extent in the case of the FeMnSiCa specimen.

The estimations of increased degradation rates for the new FeMnSiCa alloy with regards to the master FeMnSi alloy from in vitro corrosion tests agreed well with those derived from in vivo observations, thus demonstrating the powerful experimental combination offered by these two experimental approaches.

In summary, this work showed the ability of Ca-containing FeMnSi alloys to degrade at higher corrosion rates while simultaneously promoting improved osteoinduction and osseoconduction processes compared to the master FeMnSi alloy or to standard AISI 316L stainless steel.

Credit authorship contribution statement

Lucia Carmen Trincă: Data curation, Validation, Visualization, Writing – original draft, Writing – review & editing.

Liviu Burtan: Supervision; Writing - original draft; Writing – review & editing.

Daniel Mareci; Conceptualization; Methodology; Funding acquisition,

Bibiana M. Fernández-Pérez: Investigation, Formal analysis.

Iulian Stoleriu: Investigation.

Teodor Stanciu: Resources; Visualization.

Sergiu Stanciu: Investigation.

Carmen Solcan: Resources; Supervision; Writing - original draft.

Javier Izquierdo: Investigation; Data curation; Validation.

Ricardo M. Souto: Data curation, Validation, Visualization, Funding acquisition, Writing – original draft, Writing – review & editing.

Declaration of competing interest

The authors declare that they have no known competing financial interests or personal relationships that could have appeared to influence the work reported in this paper.

Acknowledgements

This work was supported partially by the Romanian National Authority for Scientific Research (CNCS-UEFISCDI, Bucharest, Romania) under project No. PN-II-IDPCE-2011-3-0218, and by the Spanish Ministry of Economy and Competitiveness (MINECO, Madrid, Spain) and the European Regional Development Fund (Brussels,

Belgium) under project No. CTQ2016-80522-P.

Appendix A. Supplementary data

Supplementary data to this article can be found online at https://doi.org/10.1016/j.msec.2020.111436.

References

[1] Y.F. Zheng, X.N. Gu, F. Witte, Biodegradable metals, Mater. Sci. Eng. R 77 (2014) 1–34, https://doi.org/10.1016/J.MSER.2014.01.001.

[2] M. Prakasam, J. Locs, K. Salma-Ancane, D. Loca, A. Largeteau, L. Berzina-Cimdina, Biodegradable materials and metallic implants — a review, J. Funct. Biomater. 8 (2017) 15, https://doi.org/10.3390/jfb8040044 44.

[3] B. Wegener, B. Sievers, S. Utzschneider, P. Müller, V. Jansson, S. Rößler, B. Nies, G. Stephani, B. Kieback, P. Quadbeck, Microstructure, cytotoxicity and corrosion of powder-metallurgical iron alloys for biodegradable bone replacement materials, Mater. Sci. Eng. B 176 (2011) 1789–1796, https://doi.org/10.1016/j.mseb.2011.04.017.

[4] M. Schinhammer, A.C. Hänzi, J.F. Löffler, P.J. Uggowitzer, Design strategy for biodegradable Fe-based alloys for medical applications, Acta Biomater. 6 (2010) 1705–1713, https://doi.org/10.1016/j.actbio.2009.07.039.

[5] M.F. Ulum, A. Arafat, D. Noviana, A.H. Yusop, A.K. Nasution, M.R. Abdul Kadir, H. Hermawan, In vitro and in vivo degradation evaluation of novel iron-bioceramic composites for bone implant applications, Mater. Sci. Eng. C 36 (2014) 336–344, https://doi.org/10.1016/j.msec.2013.12.022.

[6] J. He, F.L. He, D.W. Li, Y.L. Liu, Y.Y. Liu, Y.J. Ye, D.C. Yin, Advances in Fe-based biodegradable metallic materials, RSC Adv. 6 (2016) 112819–112838, https://doi.org/10.1039/C6RA20594A.

[7] M. Elbadawi, M. Shbeh, High strength yttria-reinforced HA scaffolds fabricated via honeycomb ceramic extrusion, J. Mech. Behav. Biomed. Mater. 77 (2018) 422–433, https://doi.org/10.1016/j.jmbbm.2017.10.009.

[8] R. Gorejová, L. Haverová, R. Oriňaková, A. Oriňak, M. Oriňak, Recent advancements in Fe-based biodegradable materials for bone repair, J. Mat. Sci. 54 (2019) 1913–1947, https://doi.org/10.1007/s10853-018-3011-z.

[9] H. Hermawan, D. Dubé, D. Mantovani, Degradable metallic biomaterials: design and development of Fe-Mn alloys for stents, J. Biomed. Mater. Res. A 93 (2010) 1–11, https://doi.org/10.1002/jbm.a.32224.

[10] H. Li, Y. Zheng, L. Qin, Progress of biodegradable metals, Prog. Nat. Sci. Mater. Int. 24 (2014) 414–422, https://doi.org/10.1016/j.pnsc.2014.08.014.

[11] T. Kraus, F. Moszner, S. Fischerauer, M. Fiedler, E. Martinelli, J. Eichler, F. Witte, E. Willbold, M. Schinhammer, M. Meischel, P.J. Uggowitzer, J.F. Löffler, A. Weinberg, Biodegradable Fe-based alloys for use in osteosynthesis: outcome of an in vivo study after 52 weeks, Acta Biomater. 10 (2014) 3346–3353, https://doi.org/10.1016/j.actbio.2014.04.007.

[12] M. Heiden, E. Walker, E. Nauman, L. Stanciu, Evolution of novel bioresorbable iron-manganese implant surfaces and their degradation behaviors in vitro, J. Biomed. Mater. Res. A 103 (2015) 185–193, https://doi.org/10.1002/jbm.a.35155.

[13] M. Bohner, Silicon-substituted calcium phosphates - a critical view, Biomaterials 30 (2009) 6403–6406, https://doi.org/10.1016/j.biomaterials.2009.08.007.

[14] A.F. Khan, M. Saleem, A. Afzal, A. Ali, A. Khan, A.R. Khan, Bioactive behavior of silicon substituted calcium phosphate based bioceramics for bone regeneration, Mater. Sci. Eng. C 35 (2014) 245–252, https://doi.org/10.1016/j.msec.2013.11.013.

[15] M. Fântânariu, L.C. Trincă, C. Solcan, A. Trofin, Ş. Strungaru, E.V. Şindilar, G. Plăvan, S. Stanciu, A new Fe-Mn-Si alloplastic biomaterial as bone grafting material: in vivo study, Appl. Surf. Sci. 352 (2015) 129–139, https://doi.org/10.1016/j.apsusc.2015.04.197.

[16] N. Cimpoeşu, L.C. Trincă, G. Dascălu, S. Stanciu, S.O. Gurlui, D. Mareci, Electrochemical characterization of a new biodegradable FeMnSi alloy coated with hydroxyapatite-zirconia by PLD technique, J. Chem. 2016 (2016) 9520972(9 pages), https://doi.org/10.1155/2016/9520972.

[17] S. Stanciu, A. Ursanu, L.C. Trincă, T.A. Elena, S. Carmen, C. Munteanu, N. Cimpoesu, D. Acatrinei, E.V. Sindilar, T. Stanciu, M. Fântânariu, Study on the biodegradability of FeMnSi alloy, Environ. Eng. Manag. J. 15 (2016) 973–980, https://doi.org/10.30638/eemj.2016.106.

[18] R. Oriňáková, A. Oriňák, L.M. Bučková, M. Giretová, L. Medveckỳ, E. Labbanczová, M. Kupková, M. Hrubovčáková, K. Koval, Iron based degradable foam structures for potential orthopedic applications, Int. J. Electrochem. Sci. 8 (2013) 12451–12465.

[19] L.C. Trincă, M. Fântânariu, C. Solcan, A.E. Trofin, L. Burtan, D.M. Acatrinei, S. Stanciu, B. Istrate, C. Munteanu, In vivo degradation behavior and biological activity of some new Mg-Ca alloys with concentration's gradient of Si for bone grafts, Appl. Surf. Sci. 352 (2015) 140–150, https://doi.org/10.1016/j.apsusc.2015.03.136.

[20] D. Hong, D.T. Chou, O.I. Velikokhatnyi, A. Roy, B. Lee, I. Swink, I. Issaev, H.A. Kuhn, P.N. Kumta, Binder-jetting 3D printing and alloy development of new biodegradable Fe-Mn-Ca/Mg alloys, Acta Biomater. 45 (2016) 375–386, https://doi.org/10.1016/j.actbio.2016.08.032.

[21] F. Săndulache, S. Stanciu, N. Cimpoeşu, T. Stanciu, R. Cimpoeşu, A. Enache, R. Baciu, Preliminary results on the surface of a new Fe-based metallic material after “in vivo” maintaining, IOP Conf. Series: Materials Science and Engineering 209 (2017) 012049, https://doi.org/10.1088/1757-899X/209/1/012049.

[22] Y. Li, H. Jahr, K. Lietaert, P. Pavanram, A. Yilmaz, L.I. Fockaert, M.A. Leeflang, B. Pouran, Y. Gonzalez-Garcia, H. Weinans, J.M.C. Mol, J. Zhou, A.A. Zadpoor, Additively manufactured biodegradable porous iron, Acta Biomater. 77 (2018) 380–393, https://doi.org/10.1016/j.actbio.2018.07.011.

[23] N. Cimpoeşu, F. Săndulache, B. Istrate, R. Cimpoeşu, G. Zegan, Electrochemical behavior of biodegradable FeMnSi–MgCa alloy, Metals 8 (2018) 15, https://doi.org/10.3390/met8070541 541.

[24] R. Drevet, Y. Zhukova, P. Kadirov, S. Dubinskiy, A. Kazakbiev, Y. Pustov, S. Prokoshkin, Tunable corrosion behavior of calcium phosphate coated Fe-Mn-Si alloys for bone implant applications, Metall. Mater. Trans. A 49 (2018) 6553–6560, https://doi.org/10.1007/s11661-018-4907-6.

[25] W. Zhang, M. Li, Q. Chen, W. Hu, W. Zhang, W. Xin, Effects of Sr and Sn on microstructure and corrosion resistance of Mg–Zr–Ca magnesium alloy for biomedical applications, Mater. Design 39 (2012) 379–383, https://doi.org/10.1016/j.matdes.2012.03.006.

[26] M. Răţoi, S. Stanciu, N. Cimpoeşu, I. Cimpoeşu, B. Constantin, C. Paraschiv, A potential biodegradable metallic material with shape memory effect based on iron, Adv. Mater. Res. 814 (2013) 110–114, https://doi.org/10.4028/www.scientific.net/AMR.814.110.

[27] MATLAB and Statistics Toolbox Release, The MathWorks, Inc., Natick, MA, 2012 (2012).

[28] B. Yeum, Electrochemical Impedance Spectroscopy: Data Analysis Software, Echem Software, Ann Arbor, MI, 2001.

[29] ISO 10993-2:2006, Biological Evaluation of Medical Devices - Part 2: Animal Welfare Requirements, International Organization for Standardization, Geneve, 2006.

[30] B. Vidal, A. Pinto, M.J. Galvão, A.R. Santos, A. Rodrigues, R. Cascão, S. Abdulghani, J. Caetano-Lopes, A. Ferreira, J.E. Fonseca, H. Canhao, Bone histomorphometry revisited, Acta Reumatol. Port. (2012) 294–300.

[31] C.A. Schneider, W.S. Rasband, K.W. Eliceiri, NIH image to ImageJ: 25 years of image analysis, Nat. Methods 9 (2012) 671–675, https://doi.org/10.1038/nmeth.2089.

[32] R.J. van't Hof, L. Rose, E. Bassonga, A. Daroszewska, Open source software for semi-automated histomorphometry of bone resorption and formation parameters, Bone 99 (2017) 69–79, https://doi.org/10.1016/j.bone.2017.03.051.

[33] M. Doube, M.M. Klosowski, I. Arganda-Carreras, F.P. Cordelières, R.P. Dougherty, J.S. Jackson, B. Schmid, J.R. Hutchinson, S.J. Shefelbine, BoneJ: free and extensible bone image analysis in ImageJ, Bone 47 (2010) 1076–1079, https://doi.org/10.1016/j.bone.2010.08.023.

[34] IBM Corp, Released 2012 IBM SPSS Statistics for Windows, Version 21.0, IBM Corp, Armonk, NY, 2012.

[35] D. Mei, S.V. Lamaka, X. Lu, M.L. Zheludkevich, Selecting medium for corrosion testing of bioabsorbable magnesium and other metals – a critical review, Corros. Sci. 171 (2020) 108722, https://doi.org/10.1016/j.corsci.2020.108722.

[36] J.R. Macdonald, Note on the parameterization of the constant-phase admittance element, Solid State Ionics 13 (1984) 147–149, https://doi.org/10.1016/0167-2738(84)90049-3.

[37] J.E.B. Randles, E. Yeager (Ed.), Transactions of the Symposium on Electrode Processes, (Philadelphia, 1959), Wiley, New York, 1961, p. 325.

[38] F.E. Heakal, A.M. Fekry, A.A. Ghoneim, Corrosion characterization of new tin–silver binary alloys in nitric acid solutions, Corros. Sci. 50 (2008) 1618–1626, https://doi.org/10.1016/j.corsci.2008.02.003/0167.

[39] A. Melillo, Rabbit clinical pathology, J. Exot. Pet Med. 16 (2007) 135–145, https://doi.org/10.1053/j.jepm.2007.06.002.

[40] I.M. Washington, G. Van Hoosier, Clinical biochemistry and hematology, in: M.A. Suckow, K.A. Stevens, R.P. Wilson (Eds.), The Laboratory Rabbit, Guinea Pig, Hamster, and Other Rodents, Academic Press, London, 2012, pp. 57–116, , https://doi.org/10.1016/B978-0-12-380920-9.00003-1.

[41] L.C. Trinca, D. Mareci, R.M. Souto, A.D. Lozano-Gorrín, J. Izquierdo, L. Burtan, I. Motrescu, V. Vulpe, G. Pavel, S. Strungaru, I. Stoleriu, A.L. Strat, C. Solcan, Osseointegration evaluation of ZrTi alloys with hydroxyapatite-zirconia-silver layer in pig's tibiae, Appl. Surf. Sci. 487 (2019) 127–137, https://doi.org/10.1016/j.apsusc.2019.05.003.

[42] L.C. Trincă, D. Mareci, C. Solcan, M. Fântânariu, L. Burtan, L. Hriţcu, C. Chiruţă, L. Fernández-Mérida, R. Rodríguez-Raposo, J.J. Santana, R.M. Souto, New Ti-6Al-2Nb-2Ta-1Mo alloy as implant biomaterial: in vitro corrosion and in vivo osseointegration evaluations, Mater. Chem. Phys. 240 (2020) 122229, https://doi.org/10.1016/j.matchemphys.2019.122229.

[43] C.P. Sousa, I.R. Dias, M. Lopez-Peña, J.A. Camassa, P.J. Lourenço, F.M. Judas, M.E. Gomes, R.L. Reis, Bone turnover markers for early detection of fracture healing disturbances: a review of the scientific literature, An. Acad. Bras. Cienc. 87 (2015) 1049–1061, https://doi.org/10.1590/0001-3765201520150008.

[44] M. Kumar, D. Shelke, S. Shah, Prognostic potential of markers of bone turnover in delayed-healing tibial diaphyseal fractures, Eur. J. Trauma Emerg. Surg. 45 (2019) 31–38, https://doi.org/10.1007/s00068-017-0879-2.

[45] J.A. Camassa, C.C. Diogo, C.P. Sousa, J.T. Azevedo, C.A. Viegas, R.L. Reis, N. Dourado, I.R. Dias, Bone turnover markers in sheep and goat: a review of the scientific literature, An. Acad. Bras. Cienc. 89 (2017) 231–245, https://doi.org/10.1590/0001-3765201720160407.

[46] B.-H. Yoon, W. Yu, Clinical utility of biochemical marker of bone turnover: fracture risk prediction and bone healing, J. Bone Metab. 25 (2018) 73–78, https://doi.org/10.11005/jbm.2018.25.2.73.

[47] M. Paskalev, N. Goranov, L. Sotirov, S. Krastev, R. Roydev, Effect of therapeutic ultrasound on bone healing and blood bone markers in dogs with experimental tibial osteotomies, Comp. Clin. Path. 21 (2012) 1593–1600, https://doi.org/10.1007/s00580-011-1333-1.

[48] P.J. Harwood, D.O. Ferguson, (ii) An update on fracture healing and non-union,

Orthop. Trauma 29 (2015) 228–242, https://doi.org/10.1016/j.mporth.2015.07.004.
[49] C. Sousa, F. Nery, J. Azevedo, C. Viegas, M. Gomes, I. Dias, Tartrate-resistant acid phosphatase as a biomarker of bone turnover in dog, Arq. Bras. Med. Vet. Zootec. 63 (2011) 40–45, https://doi.org/10.1590/S0102-09352011000100007.
[50] P. Seebeck, H.J. Bail, C. Exner, H. Schell, R. Michel, H. Amthauer, H. Bragulla, G.N. Duda, Do serological tissue turnover markers represent callus formation during fracture healing? Bone 37 (2005) 850–857, https://doi.org/10.1016/j.bone.2005.06.
[51] M.O. Coulibaly, D.L. Sietsema, T.A. Burgers, J. Mason, B.O. Williams, C.B. Jones, Recent advances in the use of serological bone formation markers to monitor callus development and fracture healing, Crit. Rev. Eukaryot. Gene Expr. 22 (2010) 629, https://doi.org/10.1016/j.bbi.2008.05.010.
[52] R. Marsell, T.A. Einhorn, The biology of fracture healing, Injury 42 (2011) 551–555, https://doi.org/10.1016/j.injury.2011.03.031.
[53] C.P. Sousa, M. Lopez-Peña, F.M. Guzón, H.V.D. Abreu, M.R. Luís, C.A. Viegas, J. Camassa, J.T.D. Azevedo, A.S. Cabrita, R.L. Reis, M.E. Gomes, I.R. Dias, Evaluation of bone turnover markers and serum minerals variations for predicting fracture healing versus non-union processes in adult sheep as a model for orthopedic research, Injury 48 (2017) 1768–1775, https://doi.org/10.1016/j.injury.2017.05.025.
[54] X. Zhang, E.M. Schwarz, D.A. Young, J. Edward Puzas, R.N. Rosier, R.J. O'Keefe, Cyclooxygenase-2 regulates mesenchymal cell differentiation into the osteoblast lineage and is critically involved in bone repair, J. Clin. Invest. 109 (2002) 1405–1415, https://doi.org/10.1172/JCI0215681.
[55] S.A. Sheweita, K.I. Khoshhal, Calcium metabolism and oxidative stress in bone fractures: role of antioxidants, Curr. Drug Metab. 8 (2007) 519–525, https://doi.org/10.2174/138920007780866852.
[56] S. Khoshniat, A. Bourgine, M. Julien, P. Weiss, J. Guicheux, L. Beck, The emergence of phosphate as a specific signaling molecule in bone and other cell types in mammals, Cell. Mol. Life Sci. 68 (2011) 205–218, https://doi.org/10.1007/s00018-010-0527-z.
[37] S. Cremers, P. Garnero, M.J. Seibel, Biochemical markers of bone metabolism, in: J.P. Bilezikian, L.G. Raisz, T.J. Martin (Eds.), Principles of Bone Biology, 3rd. edn., Academic Press, San Diego, CA, 2008, pp. 1857–1881, , https://doi.org/10.1016/B978-0-12-373884-4.00020-3.
[58] G. Cox, T.A. Einhorn, C. Tzioupis, P.V. Giannoudis, Bone-turnover markers in fracture healing, J. Bone Joint Surg. Br. 92-B (2010) 329–334, https://doi.org/10.1302/0301-620X.92B3.22787.
[59] O. Gamulin, K. Serec, V. Bilić, M. Balarin, M. Kosović, D. Drmić, L. Brčić, S. Seiwerth, P. Sikirić, Monitoring the healing process of rat bones using Raman spectroscopy, J. Mol. Struct. 1044 (2013) 308–313, https://doi.org/10.1016/j.molstruc.2013.01.049.
[60] D. Stubbs, M. Deakin, P. Chapman-Sheath, W. Bruce, J. Debes, R.M. Gillies, W.R. Walsh, In vivo evaluation of resorbable bone graft substitutes in a rabbit tibial defect model, Biomaterials 25 (2004) 5037–5044, https://doi.org/10.1016/j.biomaterials.2004.02.014.
[61] M. Mapara, B.S. Thomas, K.M. Bhat, Rabbit as an animal model for experimental research, Dent. Res. J. 9 (2012) 111–118, https://doi.org/10.4103/1735-3327.92960.
[62] Y. Li, S.K. Chen, L. Li, L. Qin, X.L. Wang, Y.X. Lai, Bone defect animal models for testing efficacy of bone substitute biomaterials, J. Orthop. Translat. 3 (2015) 95–104, https://doi.org/10.1016/j.jot.2015.05.002.
[63] Y. Hashimoto, G. Yoshida, H. Toyoda, K. Takaoka, Generation of tendon-to-bone interface "enthesis" with use of recombinant BMP-2 in a rabbit model, J. Orthop. Res. 25 (2007) 1415–1424, https://doi.org/10.1002/jor.20447.
[64] T.N. Vo, F.K. Kasper, A.G. Mikos, Strategies for controlled delivery of growth factors and cells for bone regeneration, Adv. Drug Deliv. Rev. 64 (2012) 1292–1309, https://doi.org/10.1016/j.addr.2012.01.016.
[65] M.D. Zhao, J.S. Huang, X.C. Zhang, K.K. Gui, M. Xiong, W.P. Yin, F.L. Yuan, G.P. Cai, Construction of radial defect models in rabbits to determine the critical size defects, PLoS One 11 (2016) 15, https://doi.org/10.1371/journal.pone.0146301 e0146301.
[66] W.R. Walsh, F. Vizesi, D. Michael, J. Auld, A. Langdown, R. Oliver, Y. Yu, H. Irie, W. Bruce, β-TCP bone graft substitutes in a bilateral rabbit tibial defect model, Biomaterials 29 (2008) 266–271, https://doi.org/10.1016/j.biomaterials.2007.09.035.
[67] M.L. Bouxsein, S.K. Boyd, B.A. Christiansen, R.E. Guldberg, K.J. Jepsen, R. Müller, Guidelines for assessment of bone microstructure in rodents using micro-computed tomography, J. Bone Miner. Res. 25 (2010) 1468–1486, https://doi.org/10.1002/jbmr.141.
[68] D.W. Dempster, J.E. Compston, M.K. Drezner, F.H. Glorieux, J.A. Kanis, H. Malluche, P.J. Meunier, S.M. Ott, R.R. Recker, A.M. Parfitt, Standardized nomenclature, symbols, and units for bone histomorphometry: a 2012 update of the report of the ASBMR histomorphometry nomenclature committee, J. Bone Miner. Res. 28 (2013) 2–17, https://doi.org/10.1002/jbmr.1805.
[69] S. Le Roux, F. Deschaux-Beaume, T. Cutard, P. Lours, Quantitative assessment of the interfacial roughness in multi-layered materials using image analysis: application to oxidation in ceramic-based materials, J. Europ. Ceram. Soc. 35 (2015) 1063–1079, https://doi.org/10.1016/j.jeurceramsoc.2014.09.027.
[70] E.J. Mohammad, A.M.A. Majeed, F.S. Mater, S.G. Hassan, I.A. Shaker, Image processing of SEM image nano silver using K-means MATLAB technique, Mustansiriyah J. Sci. 29 (2018) 150–157, https://doi.org/10.23851/mjs.v29i3.635.
[71] Z. Xu, M.A. Hodgson, P. Cao, Microstructure and degradation behavior of forged FeMnSi alloys, Int. J. Mod. Phys. B 29 (2015) 1540014, https://doi.org/10.1142/S0217979215400147.
[72] Y.P. Feng, A. Blanquer, J. Fornell, H. Zhang, P. Solsona, M.D. Baró, S. Suriñach, E. Ibáñez, E. García-Lecina, X. Wei, R. Li, L. Barrios, E. Pellicer, C. Nogués, J. Sort, Novel Fe-Mn-Si-Pd alloys: insights into mechanical, magnetic, corrosion resistance and biocompatibility performances, J. Mater. Chem. B 4 (2016) 6402–6412, https://doi.org/10.1039/c6tb01951j.
[73] R. Drevet, Y. Zhukova, P. Malikova, S. Dubinskiy, A. Korotitskiy, Y. Pustov, S. Prokoshkin, Martensitic transformations and mechanical and corrosion properties of Fe-Mn-Si alloys for biodegradable medical implants, Metall. Mater. Trans. A 49 (2018) 1006–1013, https://doi.org/10.1007/s11661-017-4458-2.
[74] T. Sawaguchi, L.G. Bujoreanu, T. Kikuchi, K. Ogawa, M. Koyama, M. Murakami, Mechanism of reversible transformation-induced plasticity of Fe-Mn-Si shape memory alloys, Scr. Mater. 59 (2008) 826–829, https://doi.org/10.1016/j.scriptamat.2008.06.030.
[75] B. Liu, Y.F. Zheng, L. Ruan, In vitro investigation of Fe30Mn6Si shape memory alloy as potential biodegradable metallic material, Mater. Lett. 65 (2011) 540–543, https://doi.org/10.1016/j.matlet.2010.10.068.
[76] Y.B. Ju, M. Koyama, T. Sawaguchi, K. Tsuzaki, H. Noguchi, In situ microscopic observations of low-cycle fatigue-crack propagation in high-Mn austenitic alloys with deformation-induced ε-martensitic transformation, Acta Mater. 112 (2016) 326–336, https://doi.org/10.1016/j.actamat.2016.04.042.
[77] R. Crăciun, S. Stanciu, V. Geantă, I. Voiculescu, R. Cimpoeşu, V. Manole, F. Săndulache, N. Cimpoeşu, New FeMnSi + Al alloy proposed for high damping capacity elements, Mater. Sci. Forum 907 (2017) 61–66, https://doi.org/10.4028/www.scientific.net/MSF.907.61.